
WAVEDIFFUR: A DIFFUSION SDE-BASED SOLVER FOR ULTRA MAGNIFICATION SUPER-RESOLUTION IN REMOTE SENSING IMAGES

Yue Shi, Liangxiu Han*, Darren Dancy
Department of Computing and Mathematics,
Manchester Metropolitan University
Manchester, UK
y.shi@mmu.ac.uk, l.han@mmu.ac.uk

Lianghao Han
Department of Computer Science
Brunel University
London, UK

ABSTRACT

Deep neural networks have recently achieved significant advancements in remote sensing super-resolution (SR). However, most existing methods are limited to low magnification rates (e.g., $\times 2$ or $\times 4$) due to the escalating ill-posedness at higher magnification scales. To tackle this challenge, we redefine high-magnification SR as the ultra-resolution (UR) problem, reframing it as solving a conditional diffusion stochastic differential equation (SDE). In this context, we propose WaveDiffUR, a novel wavelet-domain diffusion UR solver that decomposes the UR process into sequential sub-processes addressing conditional wavelet components. WaveDiffUR iteratively reconstructs low-frequency wavelet details (ensuring global consistency) and high-frequency components (enhancing local fidelity) by incorporating pre-trained SR models as plug-and-play modules. This modularity mitigates the ill-posedness of the SDE and ensures scalability across diverse applications. To address limitations in fixed boundary conditions at extreme magnifications, we introduce the cross-scale pyramid (CSP) constraint, a dynamic and adaptive framework that guides WaveDiffUR in generating fine-grained wavelet details, ensuring consistent and high-fidelity outputs even at extreme magnification rates. Extensive experiments demonstrate that the WaveDiffUR model, combined with CSP, achieves state-of-the-art performance by effectively minimizing degradation across key metrics: quantitative accuracy, perceptual quality, spectral consistency, and sharpness. Even when the magnification scale increases significantly from $\times 4$ to $\times 128$, the model maintains robust performance, with an average degradation of only 19.1%. At extreme magnifications (e.g., $\times 128$), it outperforms benchmark models, achieving up to 3 times the improvement in PSNR and SRE, showcasing superior image quality and spectral fidelity. By enabling robust ultra-resolution in remote sensing, WaveDiffUR opens new possibilities for applications in environmental monitoring, urban planning, disaster response, and precision agriculture. This study provides a significant step toward scalable, cost-effective, and high-fidelity solutions for real-world remote sensing challenges.

Keywords image super-resolution (SR) · diffusion model · self-cascading · wavelet transformation · cross-scale representation · remote sensing

1 Introduction

Remote sensing image super-resolution (SR) remains a persistent challenge and continues to be a vibrant research topic in both computer vision [1] and geosciences [2]. SR aims to reconstruct high-resolution (HR) remote sensing observations with realistic spectral-spatial details from low-resolution (LR) data, which are typically acquired from aerial platforms (1 - 10m resolution) or space platforms (>10 m resolution). However, current SR research predominantly focuses on fixed and low-magnification scales (e.g., $\times 2$ or $\times 4$) [3, 4, 5], which fails to meet the high-magnification scale SR demands for various Earth observation tasks. For example, land-cover mapping typically requires a spatial resolution of 1-2 meters, necessitating $\times 8$ SR for 10-meter Sentinel-2 data or $\times 16$ SR for 30-meter Landsat-8 data [6].

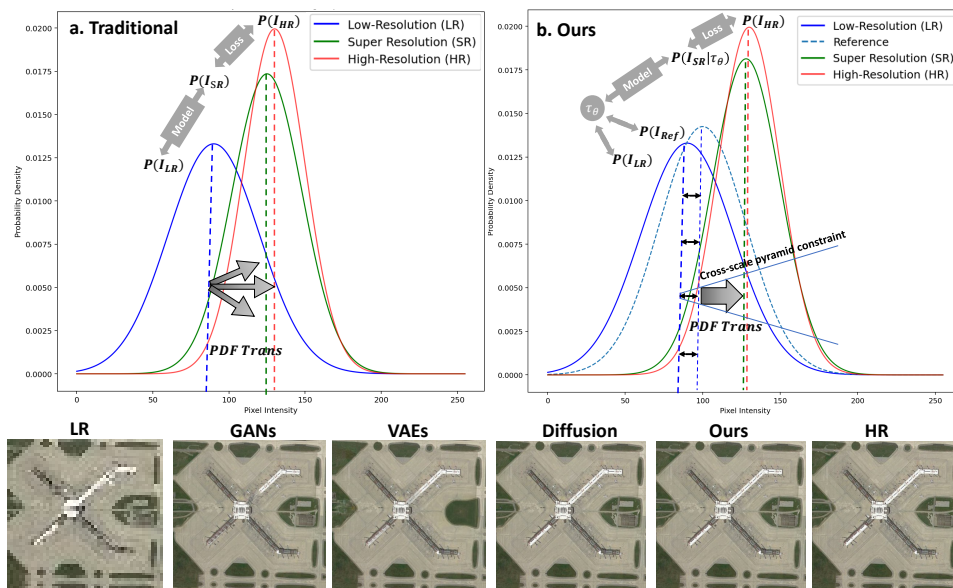


Figure 1: A comparison of SR performance across several existing PDF-based SR models using deep learning approaches, including our previous model [9].

Precision agriculture demands resolutions higher than 1 meter, translating to $\times 16$ SR for Sentinel-2 data or $\times 32$ SR for Landsat-8 data [7]. Additionally, multi-modal data fusion requires resolution matching between different data sources, which requires various scaling-rate SR enhancements ranging from $\times 4$ to $\times 64$ [8].

Unlike human or natural image super-resolution (SR), remote sensing image SR faces challenges unique to Earth Observation (EO), such as complex spatial heterogeneity and the presence of mixed pixels. These factors exacerbate the inherently ill-posed nature of SR at high-magnification scales, where the HR counterpart may exist in an infinite solution space for a given LR input [10]. Existing deep learning-based SR methods primarily address these challenges by training neural networks to model the probability density function (PDF) transition in the pixel-wise representation space, mapping the PDF of LR images to that of their HR counterparts. Fig 1 illustrates a comparison of SR performance across the most popular PDF-based SR models using deep learning approaches, including our previous model [9]. Among them, generative adversarial networks (GANs) based models use adversarial learning between a generator and a discriminator to produce SR images with realistic HR details missing in the LR images, to align the SR PDF more closely with the target HR PDF [11, 12]. Variational autoencoders (VAEs), on the other hand, encode the LR PDF into a latent space and then generate the SR image through sampling it, aiming to match the reconstructed SR PDF to that of the HR image [13]. However, due to the ill-posed nature of SR, the current models are predominantly trained on LR-HR image pairs with low magnification rates (e.g., $\times 2$ or $\times 4$), which provide effective cross-scale representations to address the problem. Our previous study [9] attempted to explore a GAN-based approach at high magnification rates. It demonstrated that when the magnification scale exceeds $\times 8$, the SR quality and fidelity diminish due to issues of mode collapse and perceptual artifacts. This decline arises from the adversarial nature of the GAN-based model, which is notoriously difficult to achieve convergence given the increased complexity of PDF transition in very large-magnification SR tasks [11]. At high magnification rates, the discontinuity of the cross-scale representations will hinder the model’s ability to maximize the likelihood of SR outputs given LR inputs. This makes the transition from the LR PDF to the HR PDF significantly more complex and less predictable.

Recently, diffusion models (DMs) [14] have received increasing attention in the field of image restoration and also demonstrated promising performance in remote sensing image SR [4, 5, 15]. The strength of diffusion models (DMs) lies in their denoising diffusion process, which gradually transforms the LR PDF into the HR PDF through a series of small, incremental noise removal steps. This process enables DMs to model high-quality SR data distributions while addressing common issues of training instability and mode collapse observed in GAN-based models, thanks to their well-defined probabilistic framework. Despite these advantages, remote sensing image SR presents a unique challenge, as it requires generating realistic and consistent spectral-spatial information across large-scale spans. Diffusion models, which are inherently based on stochastic processes, may face difficulties in consistently inferring and reconstructing the fine spectral-spatial details over extensive areas.

In this study, we introduce the concept of a cross-scale pyramid (CSP) boundary condition, which represents the unmixing rules of spectral-spatial scaling details across different magnification levels. Building on this concept, we formulate the UR process as a conditional diffusion SDE for low-frequency (fidelity) information upscaling and high-frequency (consistency) detail restoration. To solve this equation, we propose a wavelet-based diffusion UR SDE solver, named WaveDiffUR, which guides the conditional inverse diffusion process in the wavelet domain to alleviate the ill-posed nature of UR. The WaveDiffUR framework, as shown in Fig 2, enables the seamless integration of pre-trained SR pipelines as a plug-and-play module to generate the cross-scale condition, significantly reducing the costs associated with training new models from scratch. However, re-utilizing a fixed and unique condition throughout the progressive UR process may degrade the constraint capacity for solving the inverse diffusion SDE, thereby compromising the consistency and fidelity of the UR results. To address this limitation, we introduce a dynamically updated cross-scale condition, named cross-scale pyramid (CSP). The CSP serves as a variable boundary condition for the SDE solver by compressing information from adjacent UR sub-processes, guiding the WaveDiffUR solver to generate accurate UR results with realistic spectral-spatial details. Experimental results demonstrate that the baseline WaveDiffUR model without CSP exhibits high performance in terms of usability, adaptability, and cost-effectiveness. Moreover, the enhanced CSP-WaveDiffUR model effectively captures the unmixing rules of realistic spectral-spatial details, thereby improving UR efficiency and robustness in handling high-magnification SR tasks.

The primary contributions of this work are as follows:

- (i) **Pioneering the Ultra-Resolution (UR) Problem:** To the best of our knowledge, this is the first work to explicitly address the complex ill-posed UR problem. We develop a universal SDE solver, termed WaveDiffUR, which decomposes the complicated UR process into finite sub-processes. It maximizes the utilization of pre-trained SR models, enhancing the usability, adaptability, and cost-effectiveness of the UR process.
- (ii) **Dynamic Boundary Condition for the SDE solver (CSP-WaveDiffUR):** To address the degradation issue caused by re-using fixed and unique boundary conditions in constraining the diffusion UR SDE, we propose an improved version of the SDE solver, CSP-WaveDiffUR. This model dynamically updates boundary conditions during each UR sub-process, ensuring high-quality UR results with improved consistency and fidelity.
- (iii) **Extensive Experimental Validation:** Through comprehensive experiments, we validate the effectiveness of both the universal WaveDiffUR and the enhanced CSP-WaveDiffUR models and their ability to maintain UR consistency and fidelity in high-magnification UR tasks.

By addressing fundamental challenges in ultra-resolution, WaveDiffUR opens new opportunities for practical remote sensing applications, including environmental monitoring, urban planning, disaster response, and precision agriculture. This study presents a scalable, cost-effective, and high-fidelity approach to advancing remote sensing capabilities at unprecedented magnification levels.

The remainder of this paper is organized as follows: Section 2 review the related work on diffusion model and hyperspectral image super-resolution. Methodology is detailed in Section 3, including the main framework of the proposed WaveDiffUR method. Experimental results are reported in Section 4. Finally, Conclusion are presented in Section 5.

2 Related work

2.1 Remote sensing image super-resolution

To transform low-resolution remote sensing images into high-resolution counterparts, considerable efforts have been made to improve image fidelity and restoring details. Traditional methods mainly adopt fusion technologies, such as wavelet transform and spectral mixing analysis, in which the spatial information of high-resolution images can be used to improve the spatial details of low-resolution images effectively. For instance, Zhang *et al* [16] introduced an image fusion technique utilizing the 3D Wavelet Transform (3DWT). This method is particularly effective for remote sensing imaging, where the spectral dimension information is crucial, unlike in panchromatic or RGB images. The 3DWT excels in harnessing this spectral information to produce higher-quality fused images. Yokoya, *et al.* [17] proposed a coupled non-negative matrix factorization (CNMF) algorithm, based on a linear spectral mixing model. This algorithm reconstructs images with both high spatial and spectral resolution by merging low spatial resolution hyperspectral images (HSI) and high spatial resolution multispectral images (MSI), incorporating their structural features. Furthermore, realising the potential of frequency-domain gain recognition in the field of Super-Resolution (SR), Zhang *et al* [18] proposed a Bayesian estimation approach for multispectral images in the wavelet domain. This approach demonstrates strong noise resistance and consistently produces reliable fusion results, showcasing its effectiveness in handling spectral-spatial information in SR applications.

In recent years, significant advancements have been made in deep learning-based approaches to the SR problem. Dong *et al.* [19] first introduced Super-Resolution Convolutional Neural Network (SRCNN) model to learn the mapping relationship between low-resolution images (LR) and the corresponding high-resolution (HR) images, in which the LR images were produced by upscaling original LR images to the desired size using bicubic interpolation. Since then, several innovative convolutional neural network (CNN) models have been developed, emphasizing the critical role of network architecture design in enhancing image reconstruction performance of SR. For example, Muhammad, *et al.* [20] implemented a "Squeeze-and-Excitation" module to incorporate an attention mechanism targeting the channel dimension. This method utilizes a compact network designed to autonomously ascertain the significance of each channel, and then allocates network weights to each feature accordingly, enabling the network to focus on the most relevant feature channels. Similarly, Zheng, *et al.* [21] applied spatial-spectral attention mechanism to neural network models for panchromatic sharpening of hyperspectral images (HSI), allowing the networks to adaptively learn both spatial and spectral details.

In general, deep learning-based approaches in improving spatial resolution of remote sensing imaging primarily adopt two strategies: fusion with other high spatial resolution images [22, 23, 24] and single-image based SR [25, 26]. Fusion-based SR techniques utilize additional external prior information to reconstruct images with finer textures. In contrast, single-image-based SR techniques do not rely on any auxiliary data, offering greater practical feasibility. For instance, Mei *et al.* [27] developed a 3D Fully Convolutional Neural Network (3D-FCNN) model for drone image super-resolution, incorporating an upsampling process at the earlier stage. Jiang *et al.* [28] proposed the Single Sub-Image Progressive Super-Resolution (SSPSR) model, which involves progressive sampling: first for grouped sub-images and then for the entire image constructed by fusing the interpolated sub-images. This approach improves feature extraction in HSIs and enhances the stability of overall training, although it will also introduce extra requirements, such as more precise modeling and intricate network design for each stage.

The Generative Adversarial Network (GAN) is another deep learning based model that has gained significant attention in the field of super-resolution. GANs are particularly valued for their ability to model complex data distributions, enabling the generation of high-resolution (HR) images that closely mimic the quality and perceptual characteristics of real-world data. When integrated into the SR process, GANs generate HR images with enhanced visual appeal. Xiong *et al.* [29] proposed an improved Super-Resolution Generative Adversarial Network (SRGAN) with a revised loss function and optimised network architecture. These modifications improve the training stability and generalisation performance. Shi *et al.* [9] proposed the latent encoder integrated GAN, named LE-GAN, incorporating self-attention mechanisms to boost feature extraction of the generator and stabilize the training process.

In parallel, diffusion probabilistic models (DPMs) have emerged as another promising approach for super-resolution tasks. DPMs generate high-quality data distributions through a structured and well-defined probabilistic diffusion process, mitigating the training instability often seen in GANs. Recently, Saharia *et al.* [30] advanced a DPM-based super-resolution method, employing a UNet architecture as the denoiser to iteratively refine image generation. Luo *et al.* [31] further enhanced diffusion-based SR by introducing stochastic differential equations (SDEs) to better model the degradation of diffusion process. These developments underscore the potential of diffusion models for addressing complex SR challenges. A detailed investigation on diffusion-based super resolution are presented in the following section.

2.2 Diffusion-based image super-resolution

Diffusion-based models, especially denoising diffusion probabilistic models (DDPMs) [14], have emerged as a promising approach for image restoration tasks such as super-resolution [32, 33, 4], inpainting [34, 35], and deblurring [36, 37]. For example, Kawar *et al.* [38] introduced Denoising Diffusion Restoration Models (DDRM), which utilizes a pre-trained diffusion model to solve various linear inverse problems, showing superior performance across multiple image restoration tasks. Wang *et al.* [39] proposed DR2, Diffusion-Based robust degradation remover for Blind Face Restoration, which initially uses a pre-trained diffusion model for coarse degradation removal then followed by an enhancement module aiming for finer blind face restoration. Guo *et al.* [40] developed ShadowDiffusion, which leverages an unrolled diffusion model to address the challenging task of shadow removal by progressively refining results with degradation and generative priors.

The basic principle of diffusion-based image super-resolution involves the use of a Markov chain to model the transformation of high-resolution (HR) image data into noise and back again [38]. It is composed of two opposite processes: Forward process (Diffusion process) and Reverse Process (Denoising with condition). The forward process gradually corrupts an HR image through a Markov chain and transitions the HR image distribution into a stochastic (Gaussian noise) distribution by progressively adding noise. The process effectively creates a dataset of noisy images that represent the HR data in a stochastic space. In the reverse process, the HR image is reconstructed from the noisy data using the corresponding low-resolution image as a conditional factor to guide the systematic removal of noise.

The model transforms the noisy data back into the HR distribution by iteratively refining the image. Through this denoising process, the conditional diffusion model ensure the spatial and spectral consistency with the LR input while reconstructing fine details of the noisy data.

The forward noising process of diffusion-based image super-resolution can be defined with the following stochastic differential equation (SDE)[41]:

$$dx = \bar{f}(x, t)dt + \bar{g}(t)d\bar{w} \quad (1)$$

where $\bar{f}(x, t)$ is the linear drift function which governs the rate at which the HR image data x is noised in time-step t , $\bar{g}(t)$ is a scalar diffusion coefficient associated with t , and \bar{w} denotes the standard Wiener process.

Using Anderson’s theorem [42, 41], the reverse diffusion process in SR can be represented by a reverse SDE function :

$$dx = [\bar{f}(x, t) - \bar{g}(t)^2 \nabla_x \log p_t(x | y)] dt + \bar{g}(t)d\bar{w} \quad (2)$$

where x represents the reconstructed HR image, y acts as a condition that is typically derived from the LR image or intermediate features, dt denotes the infinitesimal negative time step, and \bar{w} defines the reverse Wiener process. The reverse SDE defines the generative process through the score function $\nabla_x \log p_t(x | y)$ and minimizes the following denoising score-matching objective:

$$\min_{\theta} \mathbb{E}_{t \sim U(\epsilon, 1), x_0 \sim p_0(x|y), x_t \sim p_{0,t}(x_t|x_0)} \|s_{\theta}(x_t, t) - \nabla_{x_t} \log p_{0,t}(x_t | x_0)\|_2^2 \quad (3)$$

Once the parameter θ for score function is estimated, one can replace the score function $\nabla_x \log p_t(x | y)$ in Eq. 2 with $s_{\theta}(x_t, t)$ to solve the reverse SDE.

2.3 Diffusion process in wavelet domain

The wavelet transformation is highly effective in reducing spatial dimensions while retaining critical information, setting it apart from transformation techniques like Fast Fourier Transformation (FFT) and Discrete Cosine Transform (DCT), which can suffer information loss during transformations. This advantage has led to its adoption in diffusion-based super-resolution (SR). The studies like Jiang et al [43], show the benefits of performing diffusion operations in the wavelet domain rather than directly in the image space. This approach supports improved content reconstruction and narrows the disparity between ground-truth HR and SR domains. By combining wavelet transformation with diffusion model techniques, these methods achieve enhanced super-resolution outcomes and improved performance metrics.

In 2D applications, a 2D low-resolution image, $x \in I_{LR}$, can be decomposed into four sub-bands through the 2D discrete wavelet transformation (2D-DWT) with Haar wavelet functions as follows:

$$\{A_{LR}, V_{LR}, H_{LR}, D_{LR}\} = 2D-DWT(I_{LR}) \quad (4)$$

where $A_{LR} \in \mathbb{R}^{\frac{H}{2} \times \frac{W}{2} \times c}$ is the low-frequency of the input image and $V_{LR}, H_{LR}, D_{LR} \in \mathbb{R}^{\frac{H}{2} \times \frac{W}{2} \times c}$ are respectively the vertical, horizontal, and diagonal high-frequency information of the input. Specifically, the low-frequency coefficient A_{LR} encapsulates the global consistency information of the original image, acting as a downsampled representation, while the high-frequency coefficients, V_{LR}, H_{LR} and D_{LR} , capture sparse local details which represent the fidelity details of the image. In the field of image super-resolution, images reconstructed through upscaling high-frequency coefficients largely restore the fidelity of the original images. In contrast, the low-frequency coefficient alters the global information significantly, leading to the greatest consistency with the original images. Consequently, the main objective in image super-resolution in the wavelet domain involves retrieving the low-frequency coefficient of an LR image that aligns with its high-resolution counterpart.

3 Methodology

We hypothesize that the ill-posed UR process can be modeled as a stochastic diffusion process of spectral-spatial unmixing, where the interplay between spectral fidelity and spatial consistency is systematically addressed. Our primary goal is to solve the ill-posed UR problem through a diffusion UR SDE and generate high fidelity and spatial consistent UR images from their low-resolution counterparts. The proposed UR process is generalized to a finite number of SR steps by formulating them as a solution to a conditional diffusion SDE, constrained by a pyramid-shaped multi-scale spectral-spatial unmixing rule. Inspired by Jiang *et al* [43], we adopt a wavelet domain implementation for the proposed UR process to facilitate computation efficiency. The workflow of the proposed UR approach is shown in Fig. 2. The subsequent sections will elaborate on the details of the proposed method.

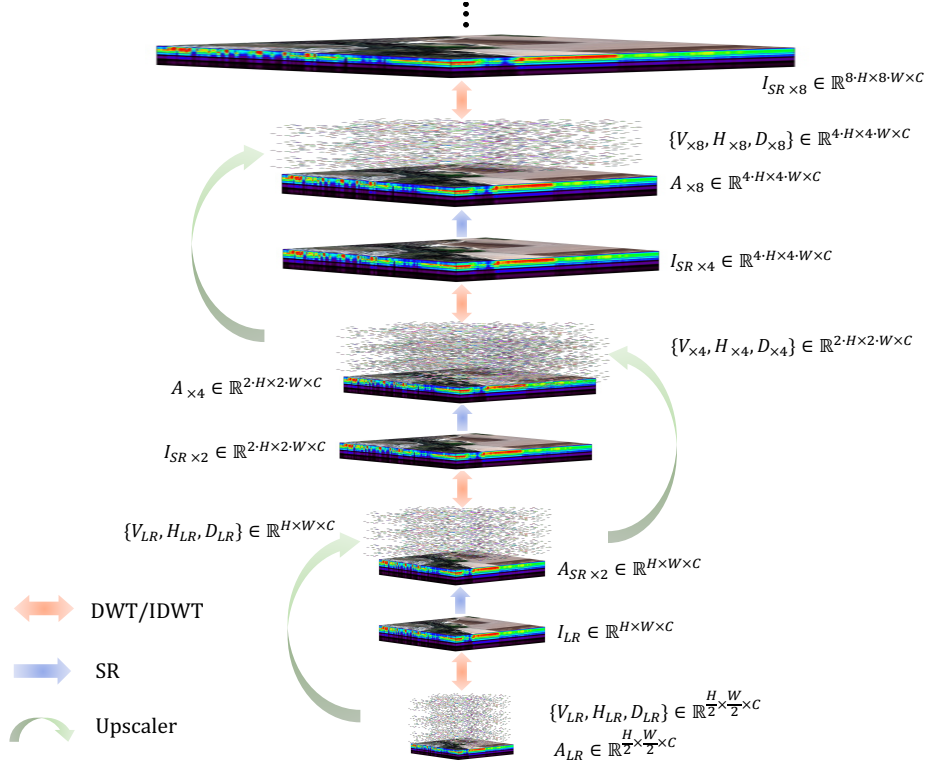


Figure 2: An Illustration of the proposed self-cascade UR pyramid framework, consisting of 1) DWT/IDWT: cyclically decompose a low-resolution image into wavelet domain, and restore the high-resolution image from the up-scaled wavelet-domain components. 2) SR pipeline: integrates a plug-and-play tunable SR module into the framework to reconstruct the low-frequency wavelet components of a high-resolution image from its low-resolution counterpart. 3) Upscaler: progressively adapts the high-frequency wavelet components of the low-resolution images to match those of the higher-resolution images.

3.1 Wavelet-domain diffusion UR (WaveDiffUR) SDE solver

The image UR process in the wavelet domain operates as a stochastic diffusion process of spectral-spatial unmixing from low-resolution space to high-resolution space. This is achieved through a series of SR steps formulated as solutions to conditional diffusion SDEs. Our proposed WaveDiffUR solver solves the conditional diffusion UR SDEs to enhance both LF and HF details. The solver ensures that spectral-spatial consistency is maintained, mitigates the ill-posed nature of the UR task by dynamically adapting to multi-scale constraints across magnification levels, and preserves the integrity of fine details during high-magnification upscaling. Each SR step iteratively refines the wavelet components, progressively generating UR wavelet components for each frequency band. LF components benefit from pre-trained SR modules to improve global structures, while HF components are upscaled to enhance texture and detail. After processing the wavelet components, Inverse Discrete Wavelet Transform (IDWT) recombines them into the spatial domain. This final reconstruction step ensures that the synthesized HR image aligns with the desired fidelity and consistency of HR ground-truth data.

Low frequency and high frequency wavelet components after DWT in WaveDiffUR can be calculated as follows:

Low-Frequency Components. The low-frequency components of the target image I_{SR} can be formulated as a function of the low-resolution image I_{LR} and the upscaling process. Mathematically, the ideal low-frequency components A_{SR} of the SR image can be expressed as:

$$A_{SR} \sim p(A_{SR}|H(I_{LR})) + \epsilon \quad (5)$$

where H is the probability density transformation function which maps I_{LR} to the domain of A_{SR} , and independent Gaussian noise ϵ accounts for uncertainties and imperfections in the transformation process. The output of $H(I_{LR})$

denotes as a condition that constraints the probability flow of A_{SR} during the UR process. The low frequency components obeys the conditional probability distribution $p(A_{SR}|H(I_{LR}))$.

However, due to the ill-posed nature of the transformation function, the analytic form of H in Eq. 5 is hard to achieve. Consequently, we use a network τ_θ to estimate the transformation function.

$$\tau_\theta(I_{LR}) = SR(p(I_{LR})) + \epsilon \rightarrow \mathbb{R}^{A_{SR}} \quad (6)$$

where $SR(p(I_{LR}))$ can be any arbitrary pre-trained SR pipeline to provide the map of $I_{LR}: \mathbb{R}^{I_{LR}} \rightarrow \mathbb{R}^{A_{SR}}$. Mathematically, $\tau_\theta(I_{LR})$ is a projection-based condition for alleviating the ill-posed problem. Thus, A_{SR} can be generated based on the conditional probability distribution, $p(A_{SR}|\tau_\theta)$. The low-frequency SR process is further formulated as a reverse diffusion SDE:

$$dA_{SR} = [\bar{f}(A_{SR,t}, t) - \bar{g}(t)^2 \nabla_{A_{SR,t}} \log p_t(A_{SR,t} | \tau_\theta(I_{LR}))] dt + \bar{g}(t) d\bar{w} \quad (7)$$

The conditional score function, $\nabla_{I_{SR}} \log p(I_{SR}|\tau_\theta(I_{LR}))$, requires model retraining whenever the cross-scale condition $\tau_\theta(I_{LR})$ is updated. This dependency limits the generalization capability of the low-frequency SR process. To address this issue, inspired by [42], we adopt an unconditional score function, $\nabla_x \log p_t(A_{SR})$, independent of $\tau_\theta(I_{LR})$. Instead, $\tau_\theta(I_{LR})$ is incorporated as an additional input or condition in the score-based framework, which guides the denoising process without constraining the model’s adaptability. More specifically, it can be described as follows:

$$A'_{SR,t-1} = f(A_{SR,t}, s_\theta) + g(A_{SR,t}) \cdot z, \quad z \sim N(0, I) \quad (8)$$

$$A_{SR,t-1} = \alpha \cdot A'_{SR,t-1} + b_t \quad (9)$$

where α, b_i are functions of $\tau_\theta(I_{LR})$ and $A_{SR,t}$. Note that Eq. 8 is identical to the unconditional reverse diffusion item in Eq. 2, whereas Eq. 9 includes the projection-based condition.

High-frequency Wavelet Components. In WaveDiffUR, the up-scaler model is tasked to transform the low-resolution wavelet component $VHD_{LR} = \{V_{LR}, H_{LR}, D_{LR}\}$ into their high-resolution counterparts $VHD_{SR} = \{V_{SR}, H_{SR}, D_{SR}\}$. The process is formulated as an up-scaling transform followed by the addition of independent Gaussian noise. The up-scaler generates VHD_{SR} as:

$$VHD_{SR} \sim \mathcal{N}(\mathbb{U}(VHD_{LR}), r^2 \mathbb{U}\mathbb{U}^\top + \sigma^2 I) \quad (10)$$

where \mathbb{U} is an upscale function, r is a standard deviation value associated with VHD_{LR} , and $\sigma^2 I$ is independent Gaussian noise. The upscale function \mathbb{U} can be estimated using a pre-trained SR model. Thus, Equation 10 is rewritten as:

$$VHD_{SR} \sim \mathcal{N}(\mathbb{U}_{SR}(VHD_{LR}), r^2 \mathbb{U}_{SR} \mathbb{U}_{SR}^\top + \sigma^2 I) \quad (11)$$

The detailed information on the WaveDiffUR method is shown in Algorithm 1.

3.2 Cross-scale pyramid (CSP) constraint WaveDiffUR solver

Considering the degradation issue of re-utilizing fixed boundary conditions $\tau_\theta(I_{LR})$ in constraining the WaveDiffUR SDE, we propose a dynamically updated boundary condition, named cross-scale pyramid (CSP), to better constraint the ill-posed problem and improve the cross-scale inference capability of τ_θ . To this end, we introduce a reference image $I_{ref} \in \mathbb{R}^{H' \times W' \times c}$, $H' \geq H$, $W' \geq W$ into our study, and the CSP condition $\tau_\theta(I_{LR}, I_{ref})$ can be modeled with joint probability $p(I_{ref}, I_{LR})$:

$$\tau_\theta(I_{LR}, I_{ref}) = T_\theta \cdot p(I_{ref}, I_{LR}) + \epsilon \rightarrow \mathbb{R}^{A_{SR}} \quad (12)$$

$\tau_\theta(I_{LR}, I_{ref})$, abbreviated as τ_θ^{lf} , ensures that the domain of the conditions at each UR level remains close to the domain of the step-wised SR target. This alignment facilitates the ill-posed inverse process in accordance with the cross-scale unmixing rule. Therefore, τ_θ^{lf} is employed as a conditional constraint to solve the inverse diffusion problem at each pyramid level. The low-frequency wavelet components of SR are expressed as:

Algorithm 1 WaveDiffUR SDE solver

```

1: input: low-resolution image  $I_{LR}$ , pre-trained SR pipeline  $SR$ , pre-trained Unet  $s_\theta$ , current resolution  $r$ , UR
   resolution  $R$ , SR rate  $k$ .
2: UR rate  $K = R/r$ , UR step  $d = K/k$ 
3: Perform a DWT
4:  $\{A_{LR}, VHD_{LR}\} = DWT(I_{LR})$ 
5:  $\tau_\theta(I_{LR}) = SR(p(I_{LR})) + \epsilon$ 
6: for  $i = 1$  to  $d$  do
7:   for  $t = T$  to  $1$  do
8:     low-frequency wavelet SR
9:      $A'_{SR,t-1} = f(A_{SR,t}, s_\theta) + g(A_{SR,t}) \cdot z$ 
10:     $A_{SR,t-1} = \alpha \cdot A'_{SR,t-1} + b_i$ 
11:   end for
12:   high-frequency wavelet restoration
13:    $VHD_{SR} \sim \mathcal{N}(\mathbb{U}_{SR}(VHD_{LR}), r^2 \mathbb{U}_{SR} \mathbb{U}_{SR}^\top + \sigma^2 I)$ 
14:    $I_{SR} = IDWT(\{A_{SR,0}, VHD_{SR}\})$ 
15:   while  $i \neq d$  do
16:      $I_{LR} = I_{SR}$ 
17:   end while
18:   while  $i = d$  do
19:      $I_{UR} = I_{SR}$ 
20:   end while
21: end for
22: output:  $I_{UR}$ 

```

$$A_{SR,t} \sim p(A_{SR,t} | \tau_\theta^{lf}) + \epsilon \quad (13)$$

It is important to note that the parameter θ evolves progressively with the increasing magnification rate, thereby enhancing the efficiency of the conditional constraint for the ill-posed inverse diffusion UR problem. Once the form of τ_θ^{lf} is identified, the fixed condition $\tau_\theta(I_{LR})$ should be replaced with it. Accordingly, the diffusion SDE for low-frequency wavelet component of SR can be solved using Eqs. 7 - 9.

To restore the sparse representations of high-frequency wavelet components (VHD_{SR}) in SR images with fidelity comparable to the HR images (VHD_{HR}), the CSP-WaveDiffUR solver employs Cross-scale Pyramid (CSP) constraints. These constraints ensure that the upscaling and inter-band interactions are guided by both the low-resolution input (VHD_{LR}) and the reference information (VHD_{ref}). The high-frequency CSP constraints are formulated in terms of $VHD_{LR} = \{V_{LR}, H_{LR}, D_{LR}\}$ and $VHD_{ref} = \{V_{ref}, H_{ref}, D_{ref}\}$ as follows:

$$\tau_\theta^V = T_{\theta_V} \cdot p(V_{LR}, V_{ref}) \quad (14)$$

$$\tau_\theta^H = T_{\theta_H} \cdot p(H_{LR}, H_{ref}) \quad (15)$$

$$\tau_\theta^D = T_{\theta_D} \cdot p(D_{LR}, D_{ref}) \quad (16)$$

where $\tau_\theta^{(\cdot)}$ are constraints for vertical (V), horizontal (H) and diagonal (D) details; $T_{\theta^{(\cdot)}}$ are transformations for the respective sub-bands and $p(\cdot)$ are cross-scale dependency modeled between low-resolution input and reference wavelet components. These constraints enhance spectral-spatial consistency by aligning the upscaled components with both the low-resolution input and reference information. The high-frequency wavelet component VHD_{SR} are restored using the CSP constraints:

$$VHD_{SR} \sim \mathcal{N}(\mathbb{M}(VHD_{LR}, \tau_\theta^{hf}), r^2 \mathbb{M} \mathbb{M}^\top + \sigma^2 I) \quad (17)$$

where \mathbb{M} is a high-frequency restoration function, which predicts sparse representations of vertical(V), horizontal(H), and diagonal (D) components of the SR image under the CSP constraints $\tau_\theta^{hf} = \{\tau_\theta^V, \tau_\theta^H, \tau_\theta^D\}$, r^2 is current resolution in

high-frequency restoration. The details of \mathbb{M} are described in Section 3.2.2. The full details about the CSP-WaveDiffUR solver is outlined in Algorithm 2. The overview of CSP-WaveDiffUR is shown in Fig. 2.

Algorithm 2 CSP-WaveDiffUR SDE solver

```

1: input: low-resolution image  $I_{LR}$ , reference image  $I_{ref}$ , pre-trained Unet  $s_\theta$ , CSP encoder  $T_\theta$ , high-frequency
   restoration module  $\mathbb{M}$ , current resolution  $r$ , UR resolution  $R$ , SR rate  $k$ .
2: UR rate  $K = R/r$ , UR step  $d = K/k$ 
3: Perform a DWT
4:  $\{A_{LR}, VHD_{LR}\} = DWT(I_{LR})$ 
5:  $\tau_\theta^{lf} = T_\theta \cdot p(I_{ref}, I_{LR}) + \epsilon$ 
6:  $\tau_\theta^{hf} = T_\theta \cdot p(hf_{ref}, hf_{LR}) + \epsilon$ 
7: for  $i = 1$  to  $d$  do
8:   for  $t = T$  to 1 do
9:     low-frequency wavelet SR
10:     $A'_{SR,t-1} = f(A_{SR,t}, s_\theta) + g(A_{SR,t}) \cdot z$ 
11:     $A_{SR,t-1} = \alpha \cdot A'_{SR,t-1} + b_i$ 
12:   end for
13:   high-frequency wavelet restoration
14:    $VHD_{SR} \sim \mathcal{N}(\mathbb{M}(VHD_{LR}, \tau_\theta^{hf}), r^2 \text{MM}^\top + \sigma^2 I)$ 
15:    $I_{SR} = IDWT(\{A_{SR,0}, VHD_{SR}\})$ 
16:   while  $i \neq d$  do
17:      $I_{LR} = I_{SR}$ 
18:   end while
19:   while  $i = d$  do
20:      $I_{UR} = I_{SR}$ 
21:   end while
22: end for
23: output:  $I_{UR}$ 

```

3.2.1 Cross-scale pyramid encoder

The Cross-Scale Pyramid Encoder (CSP Encoder) is a critical module in the CSP-WaveDiffUR framework, designed to dynamically generate cross-scale constraints for spectral-spatial unmixing. Fig. 4 illustrates the structure of the CSP encoder that models the spectral-spatial unmixing rule between a given input (\hat{x}) and its corresponding reference (\hat{x}_{ref}).

To efficiently extract the features of inputs, we use depth-wise separable convolutions [44] in the encoder. After that, the extracted features are fed into cross-attention layers to compute an intermediate representation tensor. The cross-attention mechanism leverages the information in both \hat{x} and \hat{x}_{ref} , effectively modeling the joint probability distribution $p(\hat{x} | \hat{x}_{ref})$. The intermediate representation tensor is computed as:

$$Attention(Q, K, V) = softmax\left(\frac{Q \cdot K^\top}{\sqrt{d}} \cdot V\right) \quad (18)$$

where, $Q = W_Q^{(i)} \cdot \phi_i(\hat{x}_{SR,t})$, $K = W_K^{(i)} \cdot \tau_\theta(\hat{x}, \hat{x}_{ref})$, $V = W_V^{(i)} \cdot \tau_\theta(\hat{x}, \hat{x}_{ref})$, in which $\phi_i(\hat{x}_{SR,t})$ is a flattened latent space features generated from a DeepConv block, $W_Q^{(i)}$, $W_K^{(i)}$, and $W_V^{(i)}$ are learnable projection matrices.

To enhance the representation of cross-scale spectral-spatial information, a progressive dilation Resblock is incorporated into the encoder. In this block, the first and last convolutions are utilized for local feature extraction, and a sequence of dilation convolutions are applied to expand the receptive field, capturing cross-scale dependencies.

3.2.2 High-frequency restoration module

The cross-scale high-frequency restoration (CSHR) module (Fig. 5) in CSP-WaveDiffUR is designed to reconstruct the high-frequency wavelet coefficients $\{V_{SR}, H_{SR}, D_{SR}\}$ from their low-resolution counterparts $\{V_{LR}, H_{LR}, D_{LR}\}$ and reference coefficients $\{V_{ref}, H_{ref}, D_{ref}\}$. This reconstruction enhances the vertical, horizontal, and diagonal details of the target SR image by effectively modeling cross-scale spectral-spatial interactions. The architecture of the cross-scale

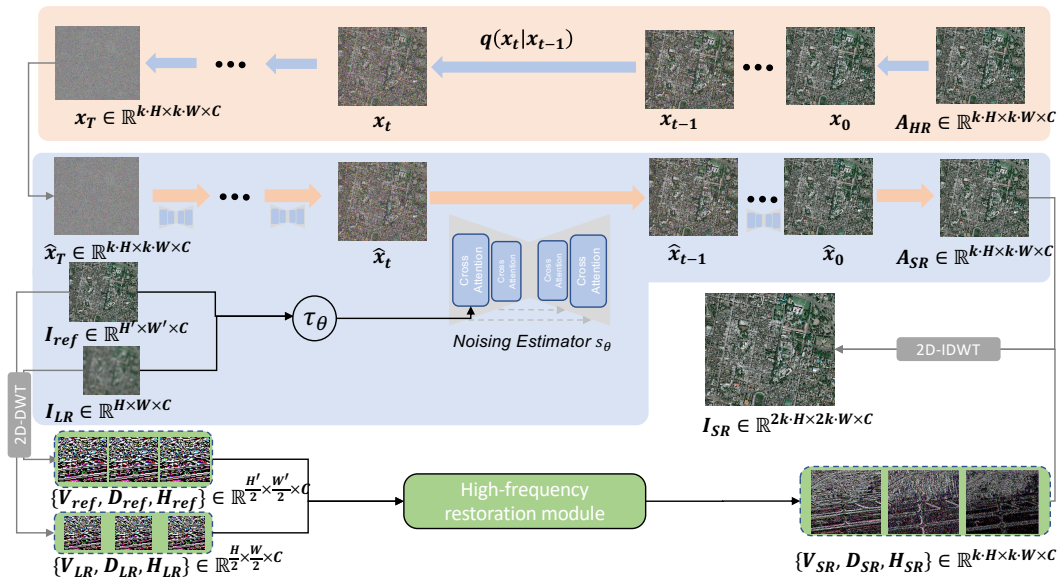


Figure 3: An overall of the proposed CSP-WaveDiffUR.

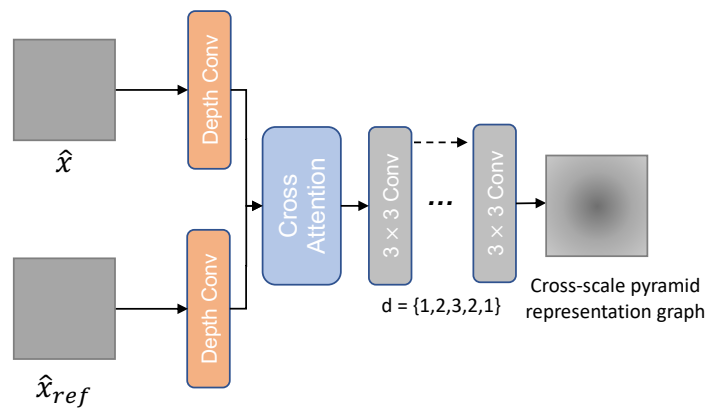


Figure 4: An illustration of the cross-scale pyramid encoder.

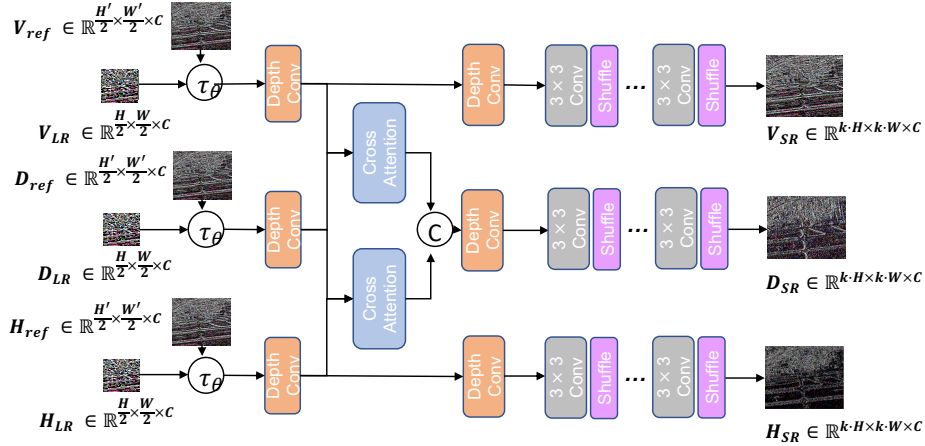


Figure 5: An illustration of the cross-scale high-frequency restoration model.

high-frequency restoration (CSHR) module is shown in Fig. 5. The module comprises the following steps: (1) Feature extraction with depth-wise separable convolutions from the input coefficients efficiently, (2) Modeling the interaction of information in V and H that augment the details in D using two cross-attention layers [45], (3) Generating SR high-frequency coefficients with a progressive dilation ResBlock developed under inspiration from the work of Hai *et al* [46], which includes a dilation convolution followed by a shuffle layer for up-scaling of high-frequency coefficients.

3.3 Model training

In addition to the objective function L_{diff} utilized for optimizing the diffusion model, a high-frequency realness loss $L_{realness}$ is employed, which combines Mean Squared Error (MSE) loss and Total Variation (TV) loss, similar to the approach described by Liu *et al.* [47]. This loss function is employed to reconstruct the high-frequency coefficients.

$$L_{realness} = \lambda_1 \|\{V_{SR}, H_{SR}, D_{SR}\} - \{V_H, H_H, D_H\}\|^2 + \lambda_2 TV(\{V_{SR}, H_{SR}, D_{SR}\}) \quad (19)$$

where $\lambda_1 = 0.1$ and $\lambda_2 = 2$ are weights for the respective terms. Moreover, we incorporate a consistent loss $L_{consistent}$ that combines $L1$ loss and SSIM loss to ensure the fidelity of the reconstructed super-resolution image I_{SR} compared to the ground truth high-resolution image I_H .

$$L_{consistent} = \|I_{SR} - I_H\| + (1 - SSIM(I_{SR} - I_H)). \quad (20)$$

The total loss for the proposed neural network can be expressed as:

$$L_{total} = L_{diff} + L_{realness} + L_{consistent} \quad (21)$$

4 Experiment and discussion

4.1 Dataset

To comprehensively evaluate the effectiveness of the methods presented in this study, we trained and fine-tuned our model on two publicly available datasets (ImageNet 1K [48], and AID [49]). In addition, we evaluated the model performance on two public datasets (DOTA [50] and DIOR [51]) and one self-designed dataset (Dataset for drone images super-resolution (DDISR)) [9]).

The details of the datasets for model training, testing and evaluation are detailed in Table 1. In the pre-training phase, ImageNet 1K was used for $(64 \times 64 \rightarrow 128 \times 128)$ super resolution tasks and the dev sets were used for validation.

Table 1: The details of the datasets for model training, testing, and evaluation.

Data type	ImageNet	AID	DOTA	DIOR	DDISR
Scale for	$\times 2$	$\times 2, \times 4$	$\times 2, \times 4$	$\times 2, \times 4$	$\times 2$ to $\times 128$
Classes	1000	30	16	20	1
Pre-train	1,281,167				
Fine-tune		8,000			
Testing	500,000	2,000			
Evaluation			480	600	300

Wherein, the original images were respectively resized to 64×64 (low-resolution), 96×96 (reference), 128×128 (high-resolution). In the fine-tuning phase, AID dataset were used for ($64 \times 64 \rightarrow 256 \times 256$) remote sensing super resolution tasks. The AID training set consisted of 8000 randomly selected images, with the remaining 2000 images as the testing set. Each image had the counterpart resolution of 64×64 , 96×96 , 256×256 . In the model testing phase, the subsets of images from the public accessible DOTA dataset and the DIOR dataset were used for model evaluation. It contains a total of 1080 images, 480 from DOTA and 600 from DIOR (30 randomly selected per class). In the data pre-processing phase, we employed bicubic interpolation for image degradation.

In real-world analysis with large scale factors, we employed the WWDSSO dataset. It consists of 300 drone-satellite synchronous observation pairs of Landset-8 image with 30m resolution (as low-resolution input), Sentinel-2 image with 10m resolution (as mid-resolution reference), and Drone image with 0.23m resolution (as ground truth). The super-resolution performance was evaluated for three scale factors $\times 10$, $\times 20$, $\times 100$. The simulated degradation was applied on ground truth drone images for scale factors ranging from $\times 2$ to $\times 128$ super-resolution.

4.2 Metrics

In this study, seven metrics were employed to comprehensively evaluate the performance of the super-resolution model. These included three full-reference metrics for assessing the similarity between super-resolution and ground-truth images: Fréchet Inception Distance (FID) [52], the widely used Peak Signal-to-Noise Ratio (PSNR), and Structural Similarity Index (SSIM) [53]. Among these, FID was extensively used to measure the generative quality of the model, improving upon the Inception Score (IS) [4] by directly measuring feature-level distances without relying on a classifier. To assess pixel-wise spectral fidelity, two metrics—Spectral Angle Mapper (SAM) and Spectral Reconstruction Error (SRE) [9]—were utilized to calculate the average angle between super-resolution images and ground-truth data. Additionally, two reference-free metrics were included: the Natural Image Quality Evaluator (NIQE) [54], which measures perceptual quality, and Average Gradient (AG), which evaluates high-frequency detail preservation. These metrics provided a holistic evaluation of the model’s performance, addressing quantitative accuracy (PSNR, SSIM), perceptual quality (FID, NIQE), spectral consistency (SAM, SRE), and sharpness (AG).

4.3 Implementation Details

The proposed model was implemented with PyTorch. The model training was conducted on three NVIDIA RTX 2080Ti GPUs. The network underwent pre-training for 1×10^4 iterations on the ImageNet 1K training dataset, and fine-tuning was performed for 1×10^3 iterations on the AID training dataset. The Adam optimizer [55] was utilized for optimization, with an initial learning rate of 1×10^{-4} , which decayed by a factor of 0.8 every 5×10^3 iterations. The batch size set to 8, and the patch size was 256×256 . The wavelet transformation scale K was set to 4 during pre-training and 8 during fine-tuning. The U-Net architecture [56] was employed as the noise estimator network in the diffusion process. To achieve efficient super-resolution, the time step T was set to 1000 during the training phase.

4.4 Model evaluation on SR tasks

To assess the performance of the proposed model, we conducted a comparative analysis. The comparative analysis included our model and several state-of-the-art (SOTA) super-resolution approaches including LE-GAN [9], ESRGAN-DP [12], RefVAE [57], LSR-SR [58], SR3 [30], IRSDE [31] EDiffSR [4], LWTDM [5]. These SOTA SR models are pre-dominant techniques within the fields, representing diverse methodologies. Specifically, LE-GAN and ESRGAN-DP represent GAN-based methods. RefVAE and LSR-SR represent VAE-based image super-resolution methods. Conversely, SR3 and IRSDE are cutting-edge diffusion-based models for natural image super-resolution. EDiffSR and LWTDM are cutting-edge diffusion-based models specific to remote sensing image super-resolution. All these comparative models were fine-tuned on the AID training dataset according to the configurations specified in their official implementations, ensuring a fair and consistent comparison.

Table 2: A quantitative comparison of the SOTA SR models pre-trained on the ImageNet dataset ($\times 2$) and fine-tuned on the AID dataset ($\times 2$, and $\times 4$) in terms of FID, PSNR, SSIM, SAM, SRE, NIQE, and AG. The tests are conducted on the dev split test data. The best values are highlighted

			ImageNet						
Category	Method	Scale	FID ↓	PSNR↑	SSIM↑	SAM ↓	SRE↓	NIQE ↓	AG ↑
GAN	LE-GAN		48.39	48.27	0.85	5.61	5.16	12.82	4.51
	ESRGAN-DP		53.26	48.02	0.84	6.97	8.35	12.24	4.81
VAE	RefVAE		47.15	45.61	0.8	7.66	9.04	13.27	4.98
	LSR-SR		47.44	45.49	0.84	7.84	8.28	12.84	5.12
Diffusion	SR3	$\times 2$	40.52	50.47	0.95	6.55	7.32	10.48	4.82
	IRSDE		45.03	48.56	0.85	6.62	7.94	12.42	5.36
	EDiffSR		40.41	49.85	0.88	6.68	7.17	11.04	5.62
	LWTDM		43.98	46.3	0.77	7.8	9.07	14.27	4.33
	Proposed		40.45	52.97	0.95	5.79	5.65	9.86	5.85
			AID						
Category	Method	Scale	FID ↓	PSNR↑	SSIM↑	SAM ↓	SRE↓	NIQE ↓	AG ↑
GAN	LE-GAN		53.13	39.8	0.71	8.09	7.68	14.3	3.9
	ESRGAN-DP		55.2	39.62	0.7	9.66	10.71	16.08	3.91
VAE	RefVAE		59.76	37.7	0.67	10.39	11.46	17.01	3.73
	LSR-SR		60.21	37.22	0.7	10.58	11.37	17.06	3.65
Diffusion	SR3	$\times 2$	51.43	40.8	0.67	10.07	10.31	13.2	3.98
	IRSDE		53.8	40.41	0.71	9.35	10.46	15.7	4.06
	EDiffSR		51.49	41.49	0.73	9.11	9.99	14.98	4.07
	LWTDM		55.06	39.56	0.64	10.72	12.03	18.04	3.65
	Proposed		50.9	41.48	0.75	8.07	7.71	12.03	4.24
GAN	LE-GAN		56.19	35.14	0.7	10.14	9.12	16.32	3.46
	ESRGAN-DP		61.05	35.64	0.63	11.31	12.75	18.67	2.82
VAE	RefVAE		66.04	33.82	0.6	12.01	13.24	19.26	3.35
	LSR-SR		66.25	32.97	0.63	11.79	13.12	19.04	3.17
Diffusion	SR3	$\times 4$	66.02	35.85	0.6	11.51	11.84	14.86	3.4
	IRSDE		59.58	35.75	0.64	11.22	11.82	17.36	2.98
	EDiffSR		56.67	37.17	0.66	10.06	11.05	16.8	3.55
	LWTDM		67.34	32.23	0.58	12.63	14.11	20.11	2.52
	Proposed		53.18	38.64	0.71	8.97	8.47	13.75	4.14

Quantitative Comparison. In the study presented, the average values of FID, PSNR, SSIM, SAM, NIQE and AG across the ImageNet and AID test sets are list in Table 2. It is observed that, for the ImageNet testing dataset, the proposed model achieves top-tier performance, ranking either 1st or showing negligible difference ($< 0.1\%$) from the top SOTA models (e.g. SR3 and EDiffSR) in FID, PSNR, and SSIM. It is noteworthy that GAN-based models, such as LE-GAN, generally excel in achieving high channel realness scores, largely due to the alignment between spectral loss computation in adversarial feature space and channel realness assessment methods, particularly for SRE. The proposed method outperforms diffusion-based models, achieving 13.12% higher SAM score than SR3. In terms of reference-free metrics (i.e. NIQE and AG), our proposed model demonstrates the best performance, underscoring its ability to preserve structural integrity in low-frequency components.

The similar results can be found when testing on the AID test dataset with a $\times 2$ scale factor. The performance of the proposed model matches EDiffSR in FID, PSNR and SSIM, is comparable with LE-GAN in SAM and SRE, and superior in NIQE and AG. For the $\times 2$ scale factor, the proposed model achieves the minimal degradation in restoration scores. The highest overall performance across all metrics demonstrates its exceptional ability to restore accurate structural details in remote sensing image super-resolution. Best NIQE and AG scores indicate the results closely align with human visual perception.

Additional results for assessing the generalization capacity of the proposed model on independent datasets are shown in Table 3, where the highest performances are highlighted in bold. The evaluation results indicate that the proposed model achieves the first place across 6 out of 7 metrics on the $\times 2$ DOTA dataset. It ranks first in all metrics on $\times 4$ DOTA dataset, and $\times 2$ and $\times 4$ DIOR datasets. The results for both $\times 2$ and $\times 4$ scale factors display consistent

Table 3: A quantitative comparison of the generalized capability between the SOTA SR models on independent DOTA and DIOR datasets for $\times 2$ and $\times 4$ super-resolution tasks in terms of FID, PSNR, SSIM, SAM, SRE, NIQE, and AG. The best values are highlighted in bold.

DOTA									
Category	Method	Scale	FID ↓	PSNR↑	SSIM↑	SAM ↓	SRE↓	NIQE ↓	AG ↑
GAN	LE-GAN		26.34	21.31	0.78	6.48	7.04	14.68	2.14
	ESRGAN-DP		26.89	21.69	0.73	9.81	10.78	17.43	3.48
VAE	RefVAE		29.65	20.27	0.81	10.99	13.27	18.67	2.28
	LSR-SR		29.46	20.26	0.8	12.51	12.73	18.22	2.09
Diffusion	SR3	$\times 2$	24.93	21.82	0.79	11.51	10.81	14.42	2.73
	IRSDE		26.82	21.9	0.7	11.17	11.96	16.63	3.07
	EDiffSR		24.92	22.66	0.71	9.21	11.03	16.77	2.58
	LWTDM		27.48	21.16	0.74	11.65	13.22	19.97	1.9
	Proposed		20.63	28.53	0.93	6.58	6.61	10.18	6.23
GAN	LE-GAN		26.72	19.55	0.72	11.86	11.41	19.37	2.06
	ESRGAN-DP		31.29	20.54	0.67	14.06	14.4	20.78	3.45
VAE	RefVAE		34.52	20.15	0.72	14.57	16.3	23.04	2.24
	LSR-SR		32.98	17.94	0.71	15.27	15.62	21.65	2.04
Diffusion	SR3	$\times 4$	27.44	20.43	0.72	13.07	15.46	18.05	2.69
	IRSDE		27.48	19.62	0.62	13.15	16.21	20.96	3.06
	EDiffSR		27.75	22.34	0.68	14.22	13.22	20.84	2.55
	LWTDM		30.31	19.87	0.59	15.2	14.15	22.34	1.87
	Proposed		22.65	28.21	0.91	7.27	7.82	11.98	6.17
DIOR									
Category	Method	Scale	FID ↓	PSNR↑	SSIM↑	SAM ↓	SRE↓	NIQE ↓	AG ↑
GAN	LE-GAN		26.09	22.71	0.79	10.11	11.75	18.97	5.41
	ESRGAN-DP		30.56	18.46	0.65	11.17	18.06	18.66	6.37
VAE	RefVAE		30.59	17.04	0.62	12.67	24.37	20.51	2.62
	LSR-SR		31.49	22.7	0.64	11.26	20.88	19.57	2.66
Diffusion	SR3	$\times 2$	27.7	23.75	0.64	13.42	18.7	18.52	3.2
	IRSDE		30.81	22.84	0.68	14.99	18.02	16.36	4.05
	EDiffSR		28.32	24.91	0.63	13.73	18.44	15.92	5.07
	LWTDM		29.35	19.05	0.65	12.78	18.09	19.78	3.25
	Proposed		21.04	27.76	0.87	9.71	8.37	15.12	7.89
GAN	LE-GAN		33.62	19.4	0.62	12.69	12.69	19.77	2.04
	ESRGAN-DP		32.97	18.65	0.59	18.38	16.39	23.13	3.44
VAE	RefVAE		36.89	17.78	0.54	13.24	19.51	19.66	2.15
	LSR-SR		35.12	17.26	0.56	16.19	15.55	22.37	1.97
Diffusion	SR3	$\times 4$	32.23	18.73	0.58	15.61	14.62	19.11	2.59
	IRSDE		32.91	17.15	0.58	15.09	13.63	21.15	2.97
	EDiffSR		27.41	18.35	0.57	14.86	15.92	22.1	2.56
	LWTDM		31.8	18.63	0.53	14.32	15.17	24.39	1.79
	Proposed		24.63	27.71	0.82	10.04	9.71	14.66	5.92

performance. The minimal performance variation across scale factors highlights the model’s robustness in handling varying resolutions. These findings confirm the proposed model’s excellent generalization capacity.

Qualitative Comparison. A visual comparison between the proposed model and the SOTA SR models is also conducted. Figure 6 demonstrates a comparisons of $\times 2$ super-resolution results ($64 \times 64 \rightarrow 128 \times 128$) on the AID, DOTA and DIOR test sets. Our proposed model consistently generates more realistic and detailed reconstruction closely resembling the ground truth image. In the case of the ”*farmland₁₄₅*” image from the AID test, the proposed model captures fine textures in farmland patches. the VAE-based models like refVAE and LWTDM show over-smoothed regions, losing critical texture details. In the case of the ”*P2541*” image from the DOTA test, the grass area reconstructed by the proposed model aligns more accurately with the ground truth, but competing models (e.g.refVAE and LSR-SR) exhibit blurred details, reflecting weaker spatial generalization. In the case of the ”*21778*” image from the DIOR test,



Figure 6: $\times 2$ visual comparisons with SOTA SR models on AID, DOTA, and DIOR test set. The square image at the left side is the input 64×64 image, and the rectangular frames indicate the zoomed-in view of the $\times 2$ super-resolution results for a better view.

the proposed model restores clear spatial details of densely built-up areas (as highlighted in the zoomed-in frames), outperforming other models like refVAE, LSR-SR, IRSDE, and LWTDM, which produce noticeable blurs.

Figure 7 provides a comparative analysis of visual results when increasing the super-resolution scale factor from $\times 2$ to $\times 4$ ($64 \times 64 \rightarrow 256 \times 256$). The analysis highlights the challenges and performance degradation by existing methods when increasing the scale factor. Most SOTA models exhibit noticeable degradation in performance. For example, blurring of fine structures in the '*baseballfield_127*' image from the AID test, such as tree crowns, road details and bridge, is prominent in VAE-based methods (e.g. RefVAE and LSR-SR) and diffusion-based methods (e.g. RSDE and LWTDM). This degradation is particularly pronounced in the DOTA and DIOR tests. More specifically, in the '*P0615*' image from the DOTA test, the bridges reconstructed by RefVAE, LSR-SR, IRSDE, and LWTDM are plagued with textural blurring. In the '*11834*' image from the DOTA test, LSR-SR and refVAE produce over-smoothed outputs, while other GAN-based and diffusion-based models provide more natural results with ground truth. However, GAN-based models like LE-GAN and ESRGAN-DP restore edge information but introduce noticeable color artefacts, diverging from the natural appearance of the ground truth. In contrast, our proposed model leverages the cross-scale pyramid architecture of the proposed model in predicting contextual prior to recover fine-grained texture, such as the details of bridge, enhancing the performance of diffusion models in super-resolution tasks.

Spectral channel evaluation. Spectral consistency is crucial in evaluating the super-resolution performance for remote sensing images. Figure 8 and Figure 9 compare the distributions of color channels (red, green and blue) for the '*P0615*' image from the DOTA test at $\times 2$ and $\times 4$ scale factors. Representative models, LE-GAN, RefVAE, and EDiffSR, are selected as benchmarks for GAN-based, VAE-based, and diffusion-based methods, respectively. It can be observed that for the $\times 2$ super-resolution task all models can adequately reproduce the spectral distributions of the ground truth in all three channels, a characteristic double-peak pattern. However, when the scale factor increase to $\times 4$, the results, as shown in Figure 9, are different. Only the proposed model maintains spectral consistency across the RFGB channels to the ground truth. The spectral distribution restored from the benchmarked models deviates from the ground truth. This observation indicates the proposed model is more robust in restoring spectral details at larger scale factors.

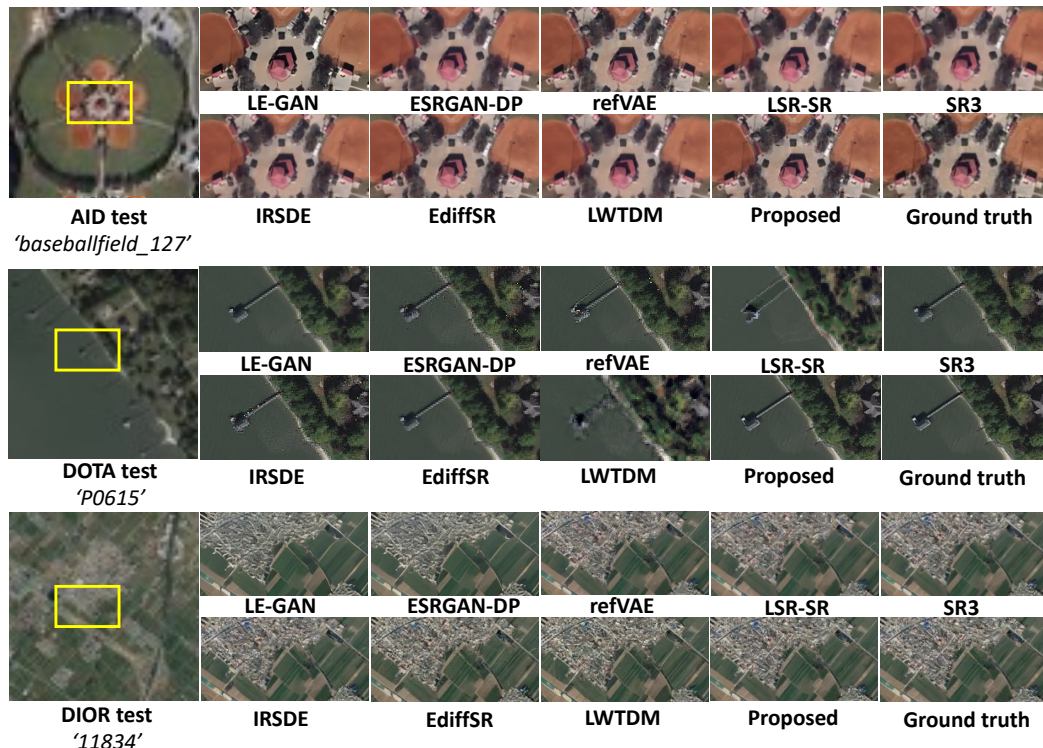


Figure 7: $\times 4$ visual comparisons with SOTA SR models on AID, DOTA, and DIOR test set. The square image at the left side is the input 64×64 image, and the rectangular frames indicate the zoomed-in view of the $\times 4$ super-resolution results for a better view.

4.5 Evaluation for UR tasks

In this section, we present the evaluation results of the proposed WaveDiffUR SDE solver for UR tasks with a $\times 2$ scale factor. Again, we used LE-GAN, refVAE, and EDiffSR as representative models from the GAN, VAE and diffusion families, respectively, serving as the upscaling modules in the WaveDiffUR framework. To further assess the effectiveness of the proposed self-cascade UR strategy, we benchmarked WaveDiffUR against a one-step UR strategy, which directly fine-tuned SR models for UR tasks. All models were tested on the DOTA and DIOR testing sets for simulated evaluation and on the DDISR dataset for real-world evaluation.

In the simulated evaluation, the DOTA and DIOR testing sets, where the highest-resolution data was treated as ground truth, and simulated lower-resolution data was generated using bicubic down-sampling. For UR resolutions beyond the highest available ground truth, pseudo ground truth images were generated by upsampling the ground truth to match the UR results for evaluation. PSNR and SRE were employed to evaluate the spatial fidelity and spectral consistency, respectively. The results are presented in Table. 4. The proposed CSP-WaveDiffUR model achieves the highest PSNR and SRE scores across all independent datasets and for all upscaling factors evaluated. It significantly outperforms its competitors, with an approximate 1.5 times improvement in PSNR and SRE for large-scale ($> \times 32$) UR. At extreme magnifications (e.g., $\times 128$), it achieves up to approximate 3 times improvement in PSNR and SRE. This is due to the Cross-Scale Pyramid (CSP) constraint in the proposed model which effectively guides the diffusion-denoising inference, enabling accurate reconstruction of both spectral and spatial details in UR tasks. Moreover, the results indicate that SR pipelines (LE-GAN, refVAE and EDDiffSR) embedded in the WaveDiffUR architecture outperform their one-step fine-tune counterparts, highlighting the benefit of the self-cascade approach. By iteratively refining UR images, the model ensures realistic inferences.

To validate the real-world applicability and generalization, we evaluated the proposed model on the real-world DDISR dataset without applying simulated degradations. As presented in Table. 4, the proposed CSP-WavediffUR model achieves the highest PSNR and SRE scores across all upscaling factors. It significantly outperforms its competitors, achieving an approximately 1.6 times improvement in PSNR and 1.8 times reduction in SRE for large-scale UR (magnifications $> \times 32$). At extreme magnifications (e.g., $\times 128$), it achieves up to a 2.8 times improvement in PSNR

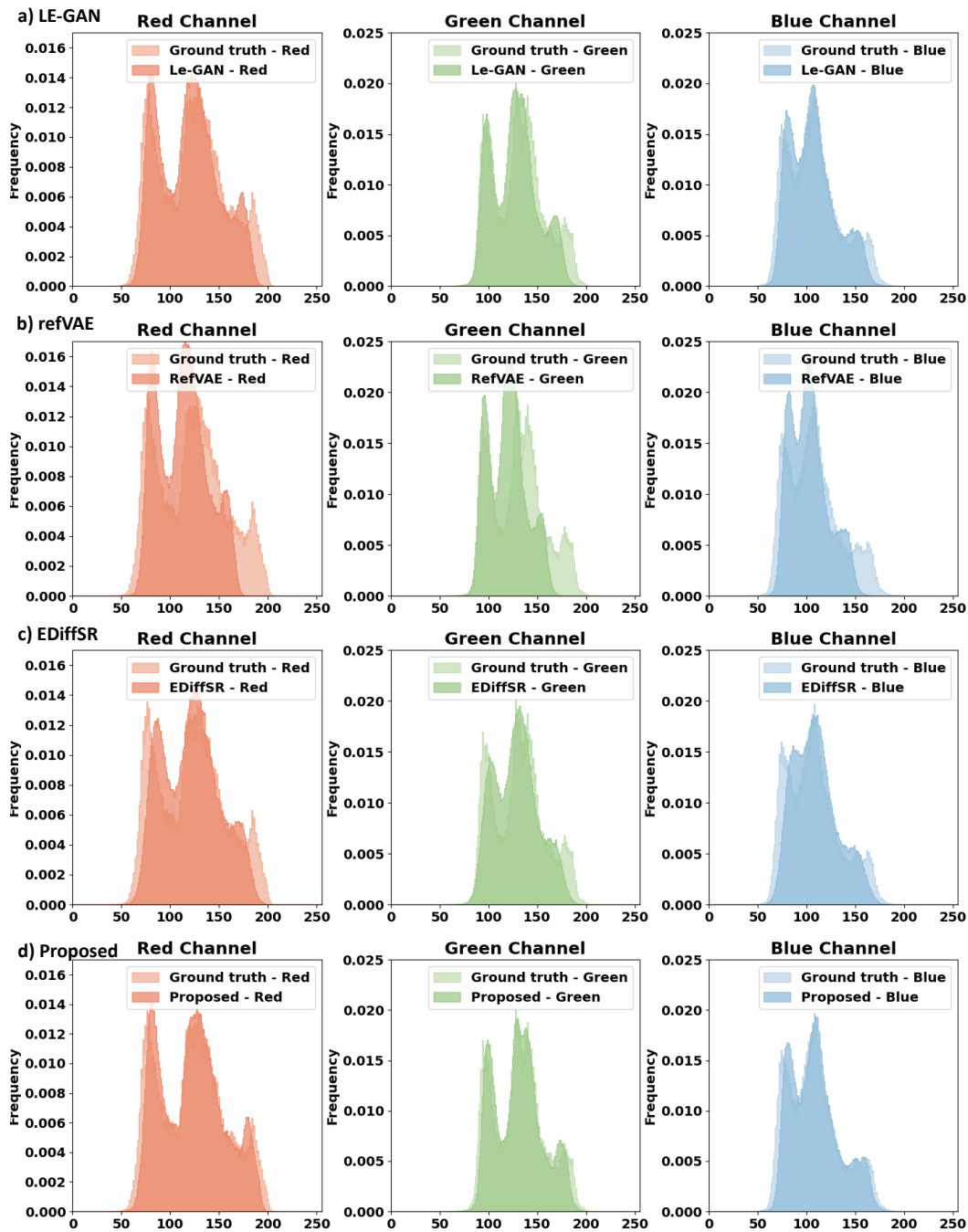


Figure 8: A comparison of spectral distributions across the red, green, blue channels between the ground truth and the $\times 2$ super-resolution image produced by a) LE-GAN, b) refVAE, c) EDiffSR, and d) proposed model for the 'P0615' image from the DOTA test. All the values in red, green, and blue channels are normalized to the range of [0, 255].

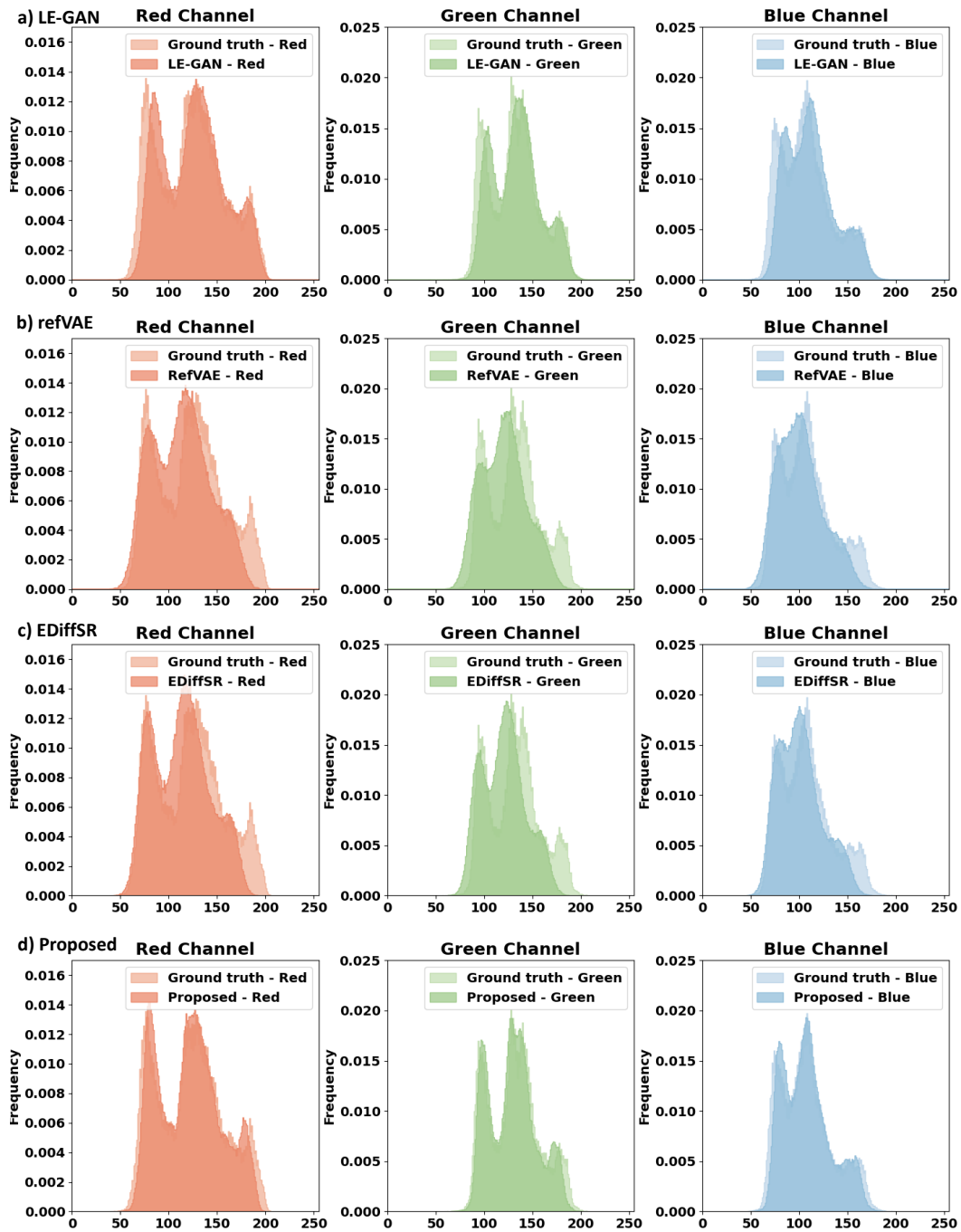


Figure 9: A comparison of spectral distributions across the red, green, blue channels between the ground truth and the $\times 4$ super-resolution image produced by a) LE-GAN, b) refVAE, c) EDiffSR, and d) proposed model for the 'P0615' image from the DOTA test. All the values in red, green, and blue channels are normalized to the range of [0, 255].

Table 4: A quantitative comparison of model performance in terms of PSNR and SRE metrics when different SR backbone models are integrated into the WaveDiffUS SDE solver for the UR tasks (scaling from $\times 4$ to $\times 128$) using the independent datasets DOTA, DIOR, and DDISR. Outputs marked with an asterisk (*) indicate evaluations are performed with pseudo ground truth images, where the UR image resolution exceeds the ground truth resolution.

DOTA						
Method	Scale					
	$\times 4$	$\times 8$	$\times 16$	$\times 32^*$	$\times 64^*$	$\times 128^*$
LE-GAN	19.15/11.41	17.11/12.88	15.91/13.32	11.53/15.42	9.21/18.89	7.91/23.33
LE-GAN-WaveDiffUR	19.74/11.39	19.18/11.12	18.21/12.86	16.74/13.40	12.58/13.63	11.21/15.87
RefVAE	22.14/14.22	22.01/15.98	20.34/16.23	16.34/18.23	12.01/23.99	10.34/30.24
RefVAE-WaveDiffUR	22.38/13.13	22.82/14.25	21.38/14.14	19.38/15.14	18.32/16.26	17.38/19.15
EDiffSR	20.15/16.31	18.92/17.31	15.15/18.32	10.15/22.32	8.92/27.32	7.15/38.33
EDiffSR-WaveDiffUR	20.02/16.51	19.29/17.02	18.02/17.52	17.25/18.21	15.99/18.35	12.02/20.53
CSP-WaveDiffUR(one-step)	28.21/7.82	28.18/7.88	26.21/9.83	21.21/12.83	19.18/17.89	18.21/19.84
CSP-WaveDiffUR	28.32/7.22	28.31/7.37	27.32/8.03	25.52/9.23	24.31/11.38	24.28/13.24
DIOR						
Method	Scale					
	$\times 4$	$\times 8$	$\times 16^*$	$\times 32^*$	$\times 64^*$	$\times 128^*$
LE-GAN	19.41/12.69	19.19/13.18	18.31/14.82	14.35/17.34	10.21/19.99	6.92/27.53
LE-GAN-WaveDiffUR	19.98/12.46	19.33/13.08	18.42/14.66	17.21/16.89	15.99/17.72	14.25/20.55
RefVAE	18.35/15.92	17.32/16.18	15.52/16.74	12.21/19.98	8.81/25.93	5.89/28.83
RefVAE-WaveDiffUR	19.01/15.28	18.99/15.82	17.59/16.11	14.49/17.52	13.21/19.14	10.15/21.71
EDiffSR	18.78/13.51	17.98/14.23	14.88/15.66	12.62/20.22	9.21/24.41	5.32/26.93
EDiffSR-WaveDiffUR	18.11/12.82	17.23/13.31	16.32/14.83	15.12/16.11	13.11/18.21	10.31/19.68
CSP-WaveDiffUR(one-step)	24.63/12.71	23.21/13.81	21.92/15.32	18.84/19.32	14.22/22.12	10.36/24.96
CSP-WaveDiffUR	25.12/8.99	24.92/9.87	22.31/9.72	21.03/10.21	18.79/12.42	16.32/14.85
DDISR						
Method	Scale					
	$\times 4$	$\times 8$	$\times 16$	$\times 32$	$\times 64$	$\times 128$
LE-GAN	24.14/16.89	21.91/18.87	19.19/21.82	16.59/24.34	12.21/28.99	8.21/32.31
LE-GAN-WaveDiffUR	24.38/15.08	23.21/16.16	23.09/16.98	19.99/19.72	16.55/22.55	14.32/26.37
RefVAE	28.12/18.18	25.52/19.74	22.11/21.81	18.81/25.93	12.89/28.23	9.82/36.20
RefVAE-WaveDiffUR	28.29/17.21	27.59/18.91	26.39/19.12	22.99/20.41	19.15/23.71	16.15/27.71
EDiffSR	28.98/23.13	27.88/26.66	24.92/29.12	19.21/34.19	13.28/39.93	12.08/38.82
EDiffSR-WaveDiffUR	29.23/21.11	28.32/22.83	27.17/23.11	25.91/24.29	21.18/25.68	18.11/28.85
CSP-WaveDiffUR(one-step)	31.21/12.19	30.92/13.39	28.84/16.32	24.22/18.12	20.36/21.62	16.13/28.21
CSP-WaveDiffUR	34.92/8.27	34.19/8.75	32.33/9.26	30.79/11.95	28.32/14.85	23.48/16.85

and SRE. Figure 10 illustrates a quantitative comparison of model performance between WaveDiffUR-based models with different backbone models (i.e. LE-GAN, EDiffSR and RefVAE), the traditional one-step fine-tune method and the proposed CSP-WaveDiffUR model for UR tasks in terms of NIQE and AG metrics. The performance degradation is observed across all models in large-scale UR tasks, but the proposed WaveDiffUR-based models with different backbone models demonstrate the most robust performance, approximately with 2.2 times better in NIQE and AG for $\times 128$ magnificant scale. The enhanced approach, CSP-WaveDiffUR, achieves the best performance in NIQE and AG (i.e. 11.8% and 19.1% performance degradation in NIQE and AG for mangificant sacle growth from $\times 4$ to $\times 128$, respectively), indicating that the proposed method can reconstruct images that contain more high-frequency detail information and align well with human perception in real-world scenarios.

To provide an intuitive comparison, we present a visual analysis of simulated and real-world evaluations. The qualitative results of the CSP-WaveDiffUR model, utilizing one-step and self-cascade strategies, are shown in Figure 11. We observe that when the UR rate is below $\times 32$, both the one-step and self-cascade approaches perform similarly, effectively recovering the overall spatial details. However, as the UR rate exceeds $\times 32$, the one-step approach begins to exhibit a blurring effect, with noticeable degradation in spatial fidelity and channel consistency, especially when compared to the self-cascade method. In the comparison of UR images with ground truth HR images at higher UR rates (such as $\times 64$ and $\times 128$), the UR images can still recover accurate details for simpler objects (e.g., white lines on the bay and embankment in simulated evaluations, or roads in real-world evaluations). However, they tend to introduce exaggerated sharpening with pseudo-details for more complex structures (e.g., boats in simulated evaluations or tree canopies in real-world evaluations). This issue is particularly noticeable with the one-step approach. A potential explanation is the

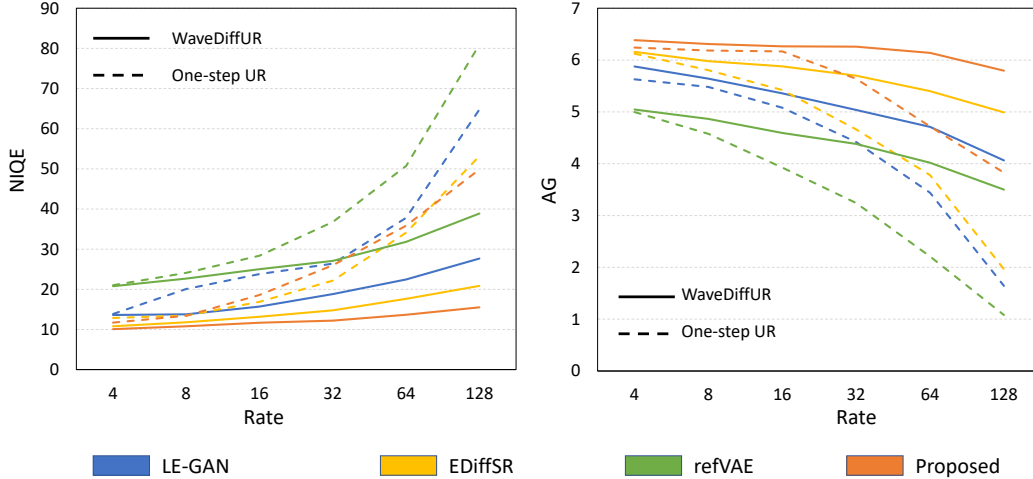


Figure 10: A comparison of model performance between WaveDiffUR-based models with different backbone models (i.e. LE-GAN, EDiffSR and RefVAE), the traditional one-step fine-tune method and the proposed CSP-WaveDiffUR model for UR tasks in terms of NIQE and AG on large-scale UR in terms of NIQE and AG.

Table 5: Ablation analysis of the proposed methodology in the $\times 8$ UR task, and the progressive self-cascade strategy is used as an example.

Model	τ_θ	High-frequency	Self-cascade	Param.(M)	FID	SRE	NIQE
Baseline				36.84	81.28	27.74	18.89
Model-1	✓			24.82	63.62	26.49	16.82
Model-2		✓		14.14	87.82	19.15	15.52
Proposed-1	✓	✓		29.12	59.15	16.24	14.33
Proposed-2	✓	✓	✓	29.12	54.82	9.81	14.03

accumulation of cross-scale biases during the transition, which hampers the realistic reconstruction of high-frequency components, leading to overly sharp, unnatural details.

4.6 Ablation Studies

In this section, we present extensive experiments to demonstrate the effectiveness of each component within our self-cascade model.

1) *Component analysis*: To evaluate the effectiveness of each component in the proposed self-cascade model, we conducted an ablation study by removing three key elements: CSP conditions, high-frequency restoration, and self-cascade structure one by one. This produced three simplified models, Baseline, Model-1 and Model-2. Table 5 summarises the model configurations and the performance evaluation results in terms of FID, SRE and NIQE. We set the upscale factor to $\times 8$ as an example. When the self-cascade architecture was excluded, the model was trained directly for the $\times 8$ upscale factor. As shown in Table 5, the evaluation results of Model-1 (with CSP condition) and the baseline diffusion model indicate that the CSP constraint significantly improves spatial fidelity (FID: 63.62 versus 81.28) while reducing model size (98.24M versus 168.14M). The evaluation results of Model-2 (with high-frequency restoration) and the baseline model display that introducing the high-frequency restoration improves channel consistency (SRE: 19.15 vs. 27.74). When both CSP constraints and the high-frequency restoration module are combined into the Proposed-1 model, a slight increase in model parameters is observed, but the FID and SRE metrics improve substantially. Embedding the Proposed-1 model into the self-cascade architecture requires no additional external parameters, as the same model is reused without fine-tuning. This integration yields significant improvements across all metrics, including FID, SRE, and NIQE. These findings demonstrate the effectiveness of the proposed methodology in enhancing large-scale image upscaling. Moreover, the low-complexity design of the components ensures that the self-cascade architecture remains both efficient and powerful.

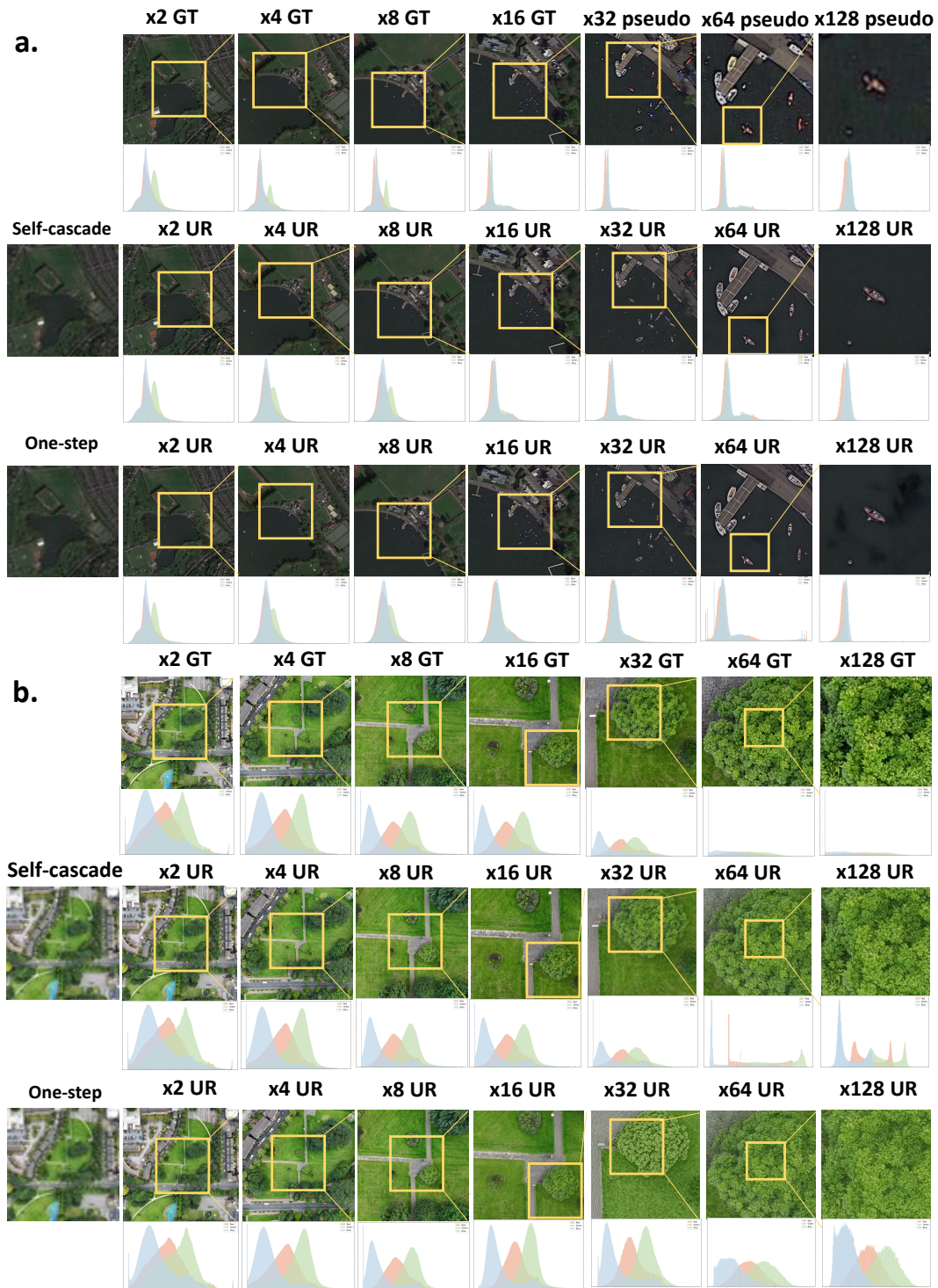


Figure 11: Visual comparisons of UR images generated from the one-step and self-cascade approaches in terms of spatial fidelity and channel consistency in a) simulated evaluation and b) real-world evaluation. For the simulated evaluation, the ground truth image is generated by zoom-in or zoom-out of the raw HR image. For the real-world evaluation, the ground truth image is collected by the multi-scale measurements. Zoom-in view in the yellow frame for a better view.

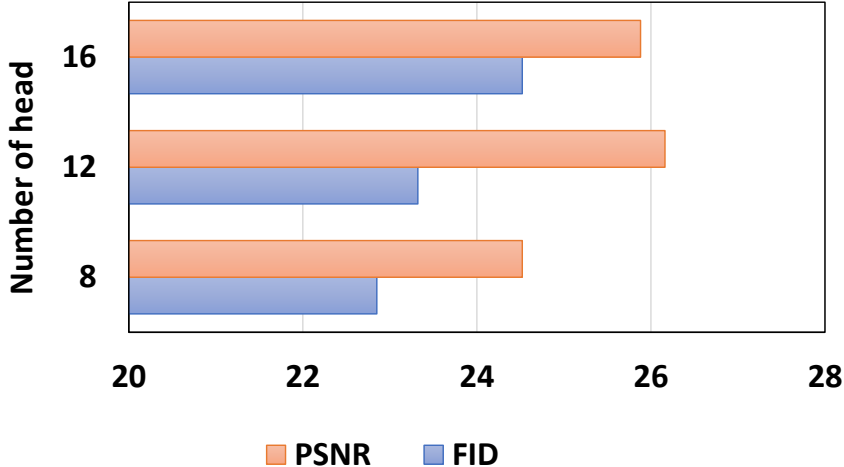


Figure 12: Ablation analysis of CSP constraint conditions with different heads of cross-attention blocks in terms of FID and SRE.

Table 6: Ablation analysis of the number of heads of the cross-attention blocks in self-cascade architecture.

	Number of head		
Models	8	12	16
Reuse	24.47/10.82	24.21/9.81	23.78/10.12
Progressive	24.12/8.99	23.92/8.87	23.71/8.91

2) *Effectiveness of CSP constraints*: We analyzed the impact of varying the number of heads in the cross-attention blocks for modeling CSP constraint conditions. As shown in Figure 12, the proposed model achieves slightly better FID performance with 16 heads compared to 12 heads, while the highest PSNR results are obtained with 12 heads. To balance model size and performance effectively, we set the default number of heads to 12.

The impact of the number of heads within the self-cascade architecture on the model performance was also conducted, 8, 12 and 16 heads were analysed in terms of FID and SRE. The experimental results, as shown in Table 6, show that the default configuration (12 heads) delivers a balanced trade-off on UR performance, optimizing both FID and SRE metrics.

3) *Effectiveness of high-frequency restoration*: To demonstrate the capability of high-frequency restoration in recovering fine details for accurate UR reconstruction, we present a visual comparison in Figure 13. Comparing the UR outputs of Model-1 (cross-scale condition-only) and Model-2 (high-frequency predictor-only), it is evident that Model-2 produces overly sharpened details compared to Model-1. Comparing the UR results of Proposed-1 and Proposed-2 within the self-cascade architecture, the combination of the high-frequency predictor and cross-scale condition achieves a superior balance between high-frequency and low-frequency components. This is particularly noticeable in features such as road edges and surface textures. These observations emphasize that the high-frequency predictor significantly enhances UR performance by predicting enriched high-frequency details with more priors, effectively improving overall reconstruction quality.

4) *Model efficiency*: To evaluate the efficiency of the self-cascade strategy, we compared the parameters and execution times of the baseline model with those of the self-cascade architecture. As shown in Figure 14, while the proposed baseline model is not the lightest among existing DPM-based SR models, it remains highly competitive in terms of efficiency.

Notably, the proposed model within the self-cascade UR architecture demonstrates faster inference speeds compared to its competitors, especially for large-scale UR tasks ($> \times 16$). This efficiency gain is primarily due to the wavelet transformation integrated into our model. By compressing the input data and processing high-frequency and low-frequency components in parallel at each UR scale, the wavelet transformation leads to reduced memory requirements for storing intermediate feature maps and fewer convolutional operations, thereby lowering computational costs. These



Figure 13: Visual ablation analysis of the $\times 128$ UR results from the model configurations listed in Table 5.

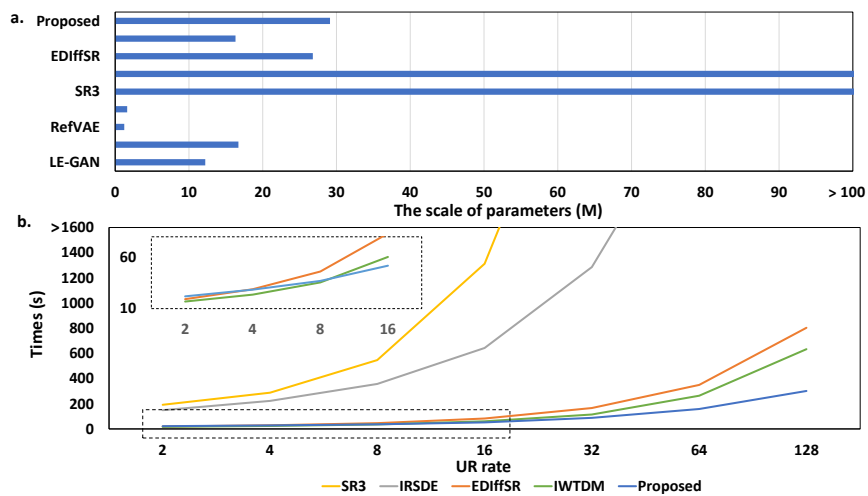


Figure 14: Model efficient comparison regarding a) the scale of baseline parameters, and b) the self-cascade model execution times with various UR rates.

optimizations enable the self-cascade architecture to outperform other approaches in computational efficiency, making our method more practical and scalable for real-world applications.

5 Conclusions

In this study, we introduce the WaveDiffUR architecture, designed to address the ill-posed challenges inherent in remote sensing super-resolution (SR) and ultra-resolution (UR) tasks. This architecture generates spectral-spatial consistent and perceptually pleasing SR and UR results for remote sensing images. Building on this foundation, the proposed CSP-WaveDiffUR model demonstrates superior performance compared to state-of-the-art (SOTA) methods in solving the UR stochastic differential equation (SDE). Unlike traditional approaches that rely on interpolated conditions, our method incorporates CSP constraint conditions, which leverage priors derived from cross-scale spectral-spatial unmixing rules. This innovation effectively mitigates the ill-posed nature of the SDE solution, resulting in mitigating degradation

across quantitative accuracy, perceptual quality, spectral consistency, and sharpness detail. Specifically, for quantitative accuracy, CSP-WaveDiffUR achieves approximately 3 times the improvement in PSNR compared to benchmark models at extreme magnifications (e.g., $\times 128$). In terms of perceptual quality and sharpness, the model demonstrates the most robust performance, with only 11.8% and 19.1% degradation in NIQE and AG metrics, respectively, as the magnification scale increases from $\times 4$ to $\times 128$, ranking first among benchmark evaluations. For spectral consistency, CSP-WaveDiffUR achieves up to 2 times reduction in SRE at $\times 128$ magnifications. Qualitative results further highlight the model's ability to preserve fine-grained details and deliver superior visual fidelity, outperforming GAN-based, VAE-based, and diffusion-based SR models.

Despite its advantages, the proposed method has certain limitations. First, the modeling of CSP constraints requires high-quality low-resolution (LR) and reference (Ref) synchronous observation pairs, which restricts its applicability in regions with sparse observational data. Second, the method does not fully account for degradation variability across different remote sensing systems, reducing its adaptability to real-world scenarios.

To address these challenges, future research will prioritize two key areas: (1) Reducing dependency on reference images by developing techniques to tackle blind super-resolution (SR) problems, thereby broadening the method's applicability in regions with limited or incomplete data; and (2) Enhancing robustness to degradation variability by designing mechanisms capable of modeling and adapting to diverse degradation patterns across different remote sensing platforms. These advancements aim to improve the robustness, adaptability, and scalability of the WaveDiffUR framework. With its demonstrated ability to outperform existing methods in accuracy and computational efficiency, the proposed approach has the potential to revolutionize applications in environmental monitoring, urban planning, disaster response, and precision agriculture, providing actionable insights at unprecedented resolutions.

Acknowledgments

This work is supported by BBSRC.(BB/Y513763/1), EPSRC (EP/X013707/1).

References

- [1] Peijuan Wang, Bulent Bayram, and Elif Sertel. A comprehensive review on deep learning based remote sensing image super-resolution methods. *Earth-Science Reviews*, 232:104110, 2022.
- [2] Xuan Wang, Jinglei Yi, Jian Guo, Yongchao Song, Jun Lyu, Jindong Xu, Weiqing Yan, Jindong Zhao, Qing Cai, and Haigen Min. A review of image super-resolution approaches based on deep learning and applications in remote sensing. *Remote Sensing*, 14(21):5423, 2022.
- [3] Jiaqing Zhang, Jie Lei, Weiying Xie, Zhenman Fang, Yunsong Li, and Qian Du. Superyolo: Super resolution assisted object detection in multimodal remote sensing imagery. *IEEE Transactions on Geoscience and Remote Sensing*, 61:1–15, 2023.
- [4] Yi Xiao, Qiangqiang Yuan, Kui Jiang, Jiang He, Xianyu Jin, and Liangpei Zhang. Ediffsr: An efficient diffusion probabilistic model for remote sensing image super-resolution. *IEEE Transactions on Geoscience and Remote Sensing*, 2023.
- [5] Tai An, Bin Xue, Chunlei Huo, Shiming Xiang, and Chunhong Pan. Efficient remote sensing image super-resolution via lightweight diffusion models. *IEEE Geoscience and Remote Sensing Letters*, 2023.
- [6] Da He, Qian Shi, Jingqian Xue, Peter M Atkinson, and Xiaoping Liu. Very fine spatial resolution urban land cover mapping using an explicable sub-pixel mapping network based on learnable spatial correlation. *Remote Sensing of Environment*, 299:113884, 2023.
- [7] Yue Shi, Liangxiu Han, Anthony Kleerekoper, Sheng Chang, and Tongle Hu. Novel cropdocnet model for automated potato late blight disease detection from unmanned aerial vehicle-based hyperspectral imagery. *Remote Sensing*, 14(02):396, 2022.
- [8] Jiang He, Qiangqiang Yuan, Jie Li, Yi Xiao, and Liangpei Zhang. A self-supervised remote sensing image fusion framework with dual-stage self-learning and spectral super-resolution injection. *ISPRS Journal of Photogrammetry and Remote Sensing*, 204:131–144, 2023.
- [9] Yue Shi, Liangxiu Han, Lianghao Han, Sheng Chang, Tongle Hu, and Darren Dancey. A latent encoder coupled generative adversarial network (le-gan) for efficient hyperspectral image super-resolution. *IEEE Transactions on Geoscience and Remote Sensing*, 60:1–19, 2022.

- [10] Huiyuan Fu, Fei Peng, Xianwei Li, Yejun Li, Xin Wang, and Huadong Ma. Continuous optical zooming: A benchmark for arbitrary-scale image super-resolution in real world. In *Proceedings of the IEEE/CVF Conference on Computer Vision and Pattern Recognition*, pages 3035–3044, 2024.
- [11] Xining Zhu, Lin Zhang, Lijun Zhang, Xiao Liu, Ying Shen, and Shengjie Zhao. Gan-based image super-resolution with a novel quality loss. *Mathematical Problems in Engineering*, 2020(1):5217429, 2020.
- [12] Jie Song, Huawei Yi, Wenqian Xu, Xiaohui Li, Bo Li, and Yuanyuan Liu. Esrgan-dp: Enhanced super-resolution generative adversarial network with adaptive dual perceptual loss. *Heliyon*, 9(4), 2023.
- [13] Zhi-Song Liu, Wan-Chi Siu, and Yui-Lam Chan. Photo-realistic image super-resolution via variational autoencoders. *IEEE Transactions on Circuits and Systems for video Technology*, 31(4):1351–1365, 2020.
- [14] Jonathan Ho, Ajay Jain, and Pieter Abbeel. Denoising diffusion probabilistic models. *Advances in neural information processing systems*, 33:6840–6851, 2020.
- [15] Jinzhe Liu, Zhiqiang Yuan, Zhaoying Pan, Yiqun Fu, Li Liu, and Bin Lu. Diffusion model with detail complement for super-resolution of remote sensing. *Remote Sensing*, 14(19):4834, 2022.
- [16] Yifan Zhang and Mingyi He. Multi-spectral and hyperspectral image fusion using 3-d wavelet transform. *Journal of electronics (China)*, 24:218–224, 2007.
- [17] Naoto Yokoya, Takehisa Yairi, and Akira Iwasaki. Coupled nonnegative matrix factorization unmixing for hyperspectral and multispectral data fusion. *IEEE Transactions on Geoscience and Remote Sensing*, 50(2):528–537, 2011.
- [18] Yifan Zhang, Steve De Backer, and Paul Scheunders. Noise-resistant wavelet-based bayesian fusion of multi-spectral and hyperspectral images. *IEEE Transactions on Geoscience and Remote Sensing*, 47(11):3834–3843, 2009.
- [19] Chao Dong, Chen Change Loy, Kaiming He, and Xiaoou Tang. Learning a deep convolutional network for image super-resolution. In *Computer Vision—ECCV 2014: 13th European Conference, Zurich, Switzerland, September 6–12, 2014, Proceedings, Part IV 13*, pages 184–199. Springer, 2014.
- [20] Wazir Muhammad, Supavadee Aramvith, and Takao Onoye. Senext: squeeze-and-excitationnext for single image super-resolution. *IEEE Access*, 2023.
- [21] Yuxuan Zheng, Jiaojiao Li, Yunsong Li, Jie Guo, Xianyun Wu, and Jocelyn Chanussot. Hyperspectral pansharpening using deep prior and dual attention residual network. *IEEE transactions on geoscience and remote sensing*, 58(11):8059–8076, 2020.
- [22] Xiongwei Zheng, Ruyi Feng, Junqing Fan, Wei Han, Shengnan Yu, and Jia Chen. Msisr-stf: Spatiotemporal fusion via multilevel single-image super-resolution. *Remote Sensing*, 15(24):5675, 2023.
- [23] Xian-Hua Han, YinQiang Zheng, and Yen-Wei Chen. Multi-level and multi-scale spatial and spectral fusion cnn for hyperspectral image super-resolution. In *Proceedings of the IEEE/CVF International Conference on Computer Vision Workshops*, pages 0–0, 2019.
- [24] Long Chen, Hui Liu, Minhang Yang, Yurong Qian, Zhengqing Xiao, and Xiwu Zhong. Remote sensing image super-resolution via residual aggregation and split attentional fusion network. *IEEE Journal of Selected Topics in Applied Earth Observations and Remote Sensing*, 14:9546–9556, 2021.
- [25] Honggang Chen, Xiaohai He, Linbo Qing, Yuanyuan Wu, Chao Ren, Ray E Sheriff, and Ce Zhu. Real-world single image super-resolution: A brief review. *Information Fusion*, 79:124–145, 2022.
- [26] Parichehr Behjati, Pau Rodriguez, Carles Fernández, Isabelle Hupont, Armin Mehri, and Jordi González. Single image super-resolution based on directional variance attention network. *Pattern Recognition*, 133:108997, 2023.
- [27] Shaohui Mei, Xin Yuan, Jingyu Ji, Yifan Zhang, Shuai Wan, and Qian Du. Hyperspectral image spatial super-resolution via 3d full convolutional neural network. *Remote Sensing*, 9(11):1139, 2017.
- [28] Junjun Jiang, He Sun, Xianming Liu, and Jiayi Ma. Learning spatial-spectral prior for super-resolution of hyperspectral imagery. *IEEE Transactions on Computational Imaging*, 6:1082–1096, 2020.
- [29] Yingfei Xiong, Shanxin Guo, Jinsong Chen, Xinpeng Deng, Luyi Sun, Xiaorou Zheng, and Wenna Xu. Improved srgan for remote sensing image super-resolution across locations and sensors. *Remote Sensing*, 12(8):1263, 2020.
- [30] Chitwan Saharia, Jonathan Ho, William Chan, Tim Salimans, David J Fleet, and Mohammad Norouzi. Image super-resolution via iterative refinement. *IEEE transactions on pattern analysis and machine intelligence*, 45(4):4713–4726, 2022.
- [31] Ziwei Luo, Fredrik K Gustafsson, Zheng Zhao, Jens Sjölund, and Thomas B Schön. Image restoration with mean-reverting stochastic differential equations. *arXiv preprint arXiv:2301.11699*, 2023.

- [32] Mengze Xu, Jie Ma, and Yuanyuan Zhu. Dual-diffusion: Dual conditional denoising diffusion probabilistic models for blind super-resolution reconstruction in rsis. *IEEE Geoscience and Remote Sensing Letters*, 2023.
- [33] Haoying Li, Yifan Yang, Meng Chang, Shiqi Chen, Huajun Feng, Zhihai Xu, Qi Li, and Yueting Chen. Srdiff: Single image super-resolution with diffusion probabilistic models. *Neurocomputing*, 479:47–59, 2022.
- [34] Yuanzhi Zhu, Kai Zhang, Jingyun Liang, Jiezhong Cao, Bihan Wen, Radu Timofte, and Luc Van Gool. Denoising diffusion models for plug-and-play image restoration. In *Proceedings of the IEEE/CVF Conference on Computer Vision and Pattern Recognition*, pages 1219–1229, 2023.
- [35] Ciprian Corneanu, Raghudeep Gadde, and Aleix M Martinez. Latentpaint: Image inpainting in latent space with diffusion models. In *Proceedings of the IEEE/CVF Winter Conference on Applications of Computer Vision*, pages 4334–4343, 2024.
- [36] Radim Spetlik, Denys Rozumnyi, and Jiří Matas. Single-image deblurring, trajectory and shape recovery of fast moving objects with denoising diffusion probabilistic models. In *Proceedings of the IEEE/CVF Winter Conference on Applications of Computer Vision*, pages 6857–6866, 2024.
- [37] Jay Whang, Mauricio Delbracio, Hossein Talebi, Chitwan Saharia, Alexandros G Dimakis, and Peyman Milanfar. Deblurring via stochastic refinement. In *Proceedings of the IEEE/CVF Conference on Computer Vision and Pattern Recognition*, pages 16293–16303, 2022.
- [38] Bahjat Kawar, Michael Elad, Stefano Ermon, and Jiaming Song. Denoising diffusion restoration models. *Advances in Neural Information Processing Systems*, 35:23593–23606, 2022.
- [39] Zhixin Wang, Ziyang Zhang, Xiaoyun Zhang, Huangjie Zheng, Mingyuan Zhou, Ya Zhang, and Yanfeng Wang. Dr2: Diffusion-based robust degradation remover for blind face restoration. In *Proceedings of the IEEE/CVF Conference on Computer Vision and Pattern Recognition*, pages 1704–1713, 2023.
- [40] Lanqing Guo, Chong Wang, Wenhan Yang, Siyu Huang, Yufei Wang, Hanspeter Pfister, and Bihan Wen. Shadowdiffusion: When degradation prior meets diffusion model for shadow removal. In *Proceedings of the IEEE/CVF Conference on Computer Vision and Pattern Recognition*, pages 14049–14058, 2023.
- [41] Yang Song, Jascha Sohl-Dickstein, Diederik P Kingma, Abhishek Kumar, Stefano Ermon, and Ben Poole. Score-based generative modeling through stochastic differential equations. *arXiv preprint arXiv:2011.13456*, 2020.
- [42] Hyungjin Chung, Byeongsu Sim, Dohoon Ryu, and Jong Chul Ye. Improving diffusion models for inverse problems using manifold constraints. *Advances in Neural Information Processing Systems*, 35:25683–25696, 2022.
- [43] Hai Jiang, Ao Luo, Haoqiang Fan, Songchen Han, and Shuaicheng Liu. Low-light image enhancement with wavelet-based diffusion models. *ACM Transactions on Graphics (TOG)*, 42(6):1–14, 2023.
- [44] François Chollet. Xception: Deep learning with depthwise separable convolutions. In *Proceedings of the IEEE conference on computer vision and pattern recognition*, pages 1251–1258, 2017.
- [45] Ruibing Hou, Hong Chang, Bingpeng Ma, Shiguang Shan, and Xilin Chen. Cross attention network for few-shot classification. *Advances in neural information processing systems*, 32, 2019.
- [46] Jiang Hai, Ren Yang, Yaqi Yu, and Songchen Han. Combining spatial and frequency information for image deblurring. *IEEE Signal Processing Letters*, 29:1679–1683, 2022.
- [47] Risheng Liu, Long Ma, Jiaao Zhang, Xin Fan, and Zhongxuan Luo. Retinex-inspired unrolling with cooperative prior architecture search for low-light image enhancement. In *Proceedings of the IEEE/CVF conference on computer vision and pattern recognition*, pages 10561–10570, 2021.
- [48] Olga Russakovsky, Jia Deng, Hao Su, Jonathan Krause, Sanjeev Satheesh, Sean Ma, Zhiheng Huang, Andrej Karpathy, Aditya Khosla, Michael Bernstein, et al. Imagenet large scale visual recognition challenge. *International journal of computer vision*, 115:211–252, 2015.
- [49] Gui-Song Xia, Jingwen Hu, Fan Hu, Baoguang Shi, Xiang Bai, Yanfei Zhong, Liangpei Zhang, and Xiaoqiang Lu. Aid: A benchmark data set for performance evaluation of aerial scene classification. *IEEE Transactions on Geoscience and Remote Sensing*, 55(7):3965–3981, 2017.
- [50] Gui-Song Xia, Xiang Bai, Jian Ding, Zhen Zhu, Serge Belongie, Jiebo Luo, Mihai Datcu, Marcello Pelillo, and Liangpei Zhang. Dota: A large-scale dataset for object detection in aerial images. In *Proceedings of the IEEE conference on computer vision and pattern recognition*, pages 3974–3983, 2018.
- [51] Ke Li, Gang Wan, Gong Cheng, Liqiu Meng, and Junwei Han. Object detection in optical remote sensing images: A survey and a new benchmark. *ISPRS journal of photogrammetry and remote sensing*, 159:296–307, 2020.

- [52] Martin Heusel, Hubert Ramsauer, Thomas Unterthiner, Bernhard Nessler, and Sepp Hochreiter. Gans trained by a two time-scale update rule converge to a local nash equilibrium. *Advances in neural information processing systems*, 30, 2017.
- [53] Zhou Wang, Alan C Bovik, Hamid R Sheikh, and Eero P Simoncelli. Image quality assessment: from error visibility to structural similarity. *IEEE transactions on image processing*, 13(4):600–612, 2004.
- [54] Anish Mittal, Rajiv Soundararajan, and Alan C Bovik. Making a “completely blind” image quality analyzer. *IEEE Signal processing letters*, 20(3):209–212, 2012.
- [55] Diederik P Kingma and Jimmy Ba. Adam: A method for stochastic optimization. *arXiv preprint arXiv:1412.6980*, 2014.
- [56] Olaf Ronneberger, Philipp Fischer, and Thomas Brox. U-net: Convolutional networks for biomedical image segmentation. In *Medical image computing and computer-assisted intervention–MICCAI 2015: 18th international conference, Munich, Germany, October 5-9, 2015, proceedings, part III 18*, pages 234–241. Springer, 2015.
- [57] Zhi-Song Liu, Wan-Chi Siu, and Li-Wen Wang. Variational autoencoder for reference based image super-resolution. In *Proceedings of the IEEE/CVF conference on computer vision and pattern recognition*, pages 516–525, 2021.
- [58] Baisong Guo, Xiaoyun Zhang, Haoning Wu, Yu Wang, Ya Zhang, and Yan-Feng Wang. Lar-sr: A local autoregressive model for image super-resolution. In *Proceedings of the IEEE/CVF conference on computer vision and pattern recognition*, pages 1909–1918, 2022.